Journal of Marine Research, 64, 355–392, 2006

On the mechanism of centennial thermohaline oscillations

by Florian Sévellec[1,2], Thierry Huck[1] and Mahdi Ben Jelloul[1]

ABSTRACT

Centennial oscillations of the ocean thermohaline circulation are studied in a 2-D latitude-depth model under mixed boundary conditions (i.e. restoring surface temperature and prescribed freshwater flux). The oscillations are revealed through linear stability analysis of a steady state obtained in a single hemisphere configuration. A density variance budget is performed and helps determine the physical processes sustaining these oscillations: the restoring surface temperature appears as a source of density variance – this is a consequence of positively-correlated temperature and salinity anomalies. A minimal model, the Howard-Malkus loop oscillator, enables us to understand physically the oscillatory and growth mechanisms. The centennial oscillation is connected to the advection of salinity anomaly around the loop; it is also related to the salinity feedback on the overturning which reinforces anomalies through a change of residence time in the freshwater flux regions. Analytical solutions of this loop model show that these centennial oscillations exist in a specific parameter regime in terms of the freshwater flux amplitude F_0: oscillations are damped if F_0 is too weak, but if F_0 is too large, the instability grows exponentially without oscillating – the latter regime is known as the positive salinity feedback. The robustness of these oscillations is then analyzed in more realistic bihemispheric configurations, some including a highly idealized Antarctic Circumpolar Current: oscillations are then always damped. These results are rationalized with the loop model, and compared to the oscillations found in general circulation models.

1. Introduction

Centennial scale variability is ubiquitous both in historical records of temperature and proxy data from sediments and ice cores – see for instance a recent review by Jones and Mann (2004). As the slow component of the Earth climate system, the ocean circulation is a potential candidate for the generation of oscillations on such long-time scales. Given the predominant centennial signal in the North Atlantic Ocean, Stocker and Mysak (1992) suggested a possible connection with the thermohaline circulation. Here we extend this idea through an analysis of ocean circulation stability in a hierarchy of simplified one- and two-dimensional (1- and 2-D) models, using linear stability analysis and density variance budgets in order to better understand the mechanism of oscillation.

1. Laboratoiré de Physique des Oceans (UMR 6523 CNRS IFREMER UBO), Universite de Bretagne Occidentale, UFR Sciences, 6 Avenue Le Gorgeu, CS 93837, 29238 Brest Cedex 3, France.
2. Corresponding author. ***email: florian.sevellec@univ-brest.fr***

Centennial scale variability is found in ocean general circulation models forced by various surface boundary conditions, stochastic forcing included (Mikolajewicz and Maier-Reimer, 1990). In a more idealized single-hemisphere flat-bottom geometry, Winton and Sarachik (1993) used both 3-D and 2-D models to investigate the oscillations mechanism and suggested the use of the simple Howard-Malkus loop oscillator as prototype. Mysak *et al.* (1993) described these centennial oscillations in a double-hemisphere 2-D model forced by mixed boundary conditions and addition of a stochastic freshwater flux. Similar oscillations also appear in box-models and rely on the strength of the freshwater flux under mixed boundary conditions (Tziperman *et al.*, 1994).

The bifurcation structure of such 2-D thermohaline circulations has been widely investigated (Quon and Ghil, 1995; Dijkstra and Molemaker, 1997). In a double-hemisphere basin symmetrically-forced by prescribed SST and freshwater flux, the symmetry breaking of both thermally- and salinity-driven double-cell flows results from asymmetric salt transports. Depending on the freshwater shape, Hopf bifurcation may occur and lead to limit cycle with periods of about the overturning time scale, where the salinity perturbations mainly drive the oscillatory flow.

For oscillations occurring around a steady state, linear stability analysis is a classical and powerful tool to get insight into the transitions to variability and their mechanism. Huck and Vallis (2001) used an empirical linearization in 3-D ocean models to study the interdecadal ocean variability under constant surface heat flux. To extend this study Te Raa and Dijkstra (2002) used a proper continuation method together with linear stability analysis, and confirmed a "generalized" large-scale baroclinic instability mechanism in agreement with a suggestion by Colin de Verdière and Huck (1999).

Te Raa and Dijkstra (2003) also investigated the mechanism of centennial oscillations, using linear stability analysis and continuation methods in 3-D and 2-D models. They related 3-D oscillations with centennial periods to 2-D oscillations with millennial scales (maybe because the mean overturning is then reduced from 20 to 5 Sv). They also found, from mean advection processes, that oscillations with active salinity, but uniform mean background salinity field, were quite similar to the ones with no salinity despite a reduced damping and a longer period. The focus here will be on a case with active salinity and a prescribed freshwater flux that sets up a nonuniform mean salinity field. By extending the linear stability analysis to a global model, Weijer and Dijkstra (2003) found a damped global mode of millennial period. It is worth noting that these studies were all conducted with a rather large horizontal viscosity responsible for an elevation of the damping rate, even though this increase was limited for the large-scale mode.

The long history in oceanography of the Howard-Malkus loop oscillator proposed as a prototype for centennial oscillations is likely dated back to the U-shaped thermal oscillator discussed by Welander (1957). Its geometry has been adapted to resemble the oceanic thermohaline circulation; it seems that the seminal loop oscillator was initially designed during Welander's stay at WHOI (Welander, 1965; Keller, 1966; Welander, 1967). The

original Howard-Malkus model dates from the GFD summer school held at Woods Hole in 1971 (Howard, 1971), and the model has also been applied to the turbulence of the thermohaline circulation "à la Lorenz" (Malkus, 1972).

Two decades later, Dewar and Huang (1996) and Huang and Dewar (1996) investigated the stability of the salinity-driven circulation with respect to different formulations of surface fluxes, i.e. natural boundary conditions as introduced by Huang (1993), virtual salt flux and restoring boundary conditions, applied to a weakly frictional loop model. As for us, we expect the ocean circulation to be strongly damped on centennial time scales (Dewar and Huang, 1995) and to be primarily thermally-driven.

The present study was aimed at constituting part of a systematic description of several types of oscillations occurring in ocean models and made with similar objective methods (linear stability analysis, density variance budget, reduced order models). Arzel (2004) and Arzel *et al.* (2006) provided the first trial of this methodology by differentiating two types of interdecadal thermohaline oscillations in 3-D ocean models; indeed, some of them were identified as related to intrinsic ocean large-scale baroclinic instability, the other to mixed surface boundary conditions. This systematic approach should enable us to unambiguously determine the nature of oscillations occurring in more realistic and/or coupled models. Here, the same methodology is applied to the centennial oscillations of the thermohaline circulation under mixed boundary conditions in a 2-D ocean model and a loop model.

The paper is organized as follows: The 2-D ocean model is described in Section 2. Section 3 deals with the numerical experiments carried out in a single-hemisphere configuration where centennial oscillations can develop; it also describes the linear stability analysis and shows its ability to accurately provide the oscillation periods and damping/growth rates. The physical processes implied in the oscillations are identified through a detailed density variance budget. These qualify the Howard-Malkus loop model as a minimal system for reproducing the oscillations (Section 4): nonlinear integrations and analytical linear stability analysis provide some more insight in the physical mechanism of the oscillations. The robustness of the centennial oscillations is then tested in a bihemispheric pole-to-pole configuration, with and without an idealized Antarctic Circumpolar Channel (Section 5). Conclusions are drawn in Section 6.

2. The ocean model

For time scales much longer than the adjustment time of an ocean basin, which is of order of decades given baroclinic Rossby wave speed at midlatitudes, the ocean dynamics is in balance with the density field even in zonal average. For the centennial timescales of interest here, a zonally-averaged 2-D model of the ocean circulation, where a single overturning streamfunction is sufficient to capture the dynamics, is clearly appropriate (Winton and Sarachik, 1993; Te Raa and Dijkstra, 2003). The model equations and forcing are described hereafter.

a. Model equations

The latitude-depth 2-D model is based on the 3-D planetary geostrophic equations in Cartesian coordinates with a linearized equation of state for the seawater:

$$f\mathbf{k}\times\mathbf{u} = -\frac{\nabla P}{\rho_0} - \frac{\rho g\mathbf{k}}{\rho_0} + \mathcal{D}, \tag{1}$$

$$\rho = \rho_0[1 - \alpha(T - T_0) + \beta(S - S_0)], \tag{2}$$

where $\mathbf{k}$ is the unit vector pointing upward, f is the Coriolis parameter, $\mathbf{u}$ is the velocity, P is the pressure, $\mathcal{D}$ is the friction term which will be discussed later, ρ (ρ_0) is the (reference) density, α is the thermal expansion coefficient, T (T_0) is the (reference) temperature, β is the haline contraction coefficient, and S (S_0) is the (reference) salinity.

The thermodynamic equations are the same as in the primitive equations and are readily transformed in two dimensions as follows:

$$\partial_t T = -J(\psi, T) + K_H\partial_y^2 T + K_V\partial_z^2 T + \mathcal{F}_T + \mathcal{C}_T, \tag{3a}$$

$$\partial_t S = -J(\psi, S) + K_H\partial_y^2 S + K_V\partial_z^2 S + \mathcal{F}_S + \mathcal{C}_S, \tag{3b}$$

where y is the latitude (in km), z is the vertical coordinate, T is the temperature, S is the salinity, J is the Jacobian operator, ψ is the overturning streamfunction defined as $\bar{w} = \partial_y\psi$ and $\bar{v} = -\partial_z\psi$ (where the overbar denotes the zonal average), K_H (K_V) is the horizontal (vertical) eddy diffusivity, $\mathcal{F}$ is the forcing term and $\mathcal{C}$ is the convection term. Convection sets in if $\partial_z\rho > 0$ and instantaneously mixes T and S downward (while conserving total heat and salt content) until a stable profile is achieved.

In a 2-D model, zonal averaging requires some dynamical approximations (Wright *et al.*, 1995, 1998). Marotzke *et al.* (1988) used Fickian vertical eddy viscosity for the friction term ($A\partial_z^2\mathbf{u}$), but with an enhanced vertical viscosity, A^*, based on the hypothesis that the overturning is proportional to the nonrotating approximation one. Wright and Stocker (1991) set the east-west pressure difference proportional to the meridional gradient of zonally-averaged pressure and used a vertical eddy viscosity for the friction term. Application of the same method together with the replacement of vertical eddy viscosity with a linear friction provided us with a much simpler system (especially for the linearization):

$$\frac{1}{\rho_0}\partial_y\overline{P} = -\varepsilon\bar{v}, \tag{4}$$

where $\varepsilon = 1.45\times10^{-4}\ \mathrm{s}^{-1}$ was such that the obtained overturning is reasonable for a typical North Atlantic thermohaline stratification. This solution corresponds to a very frictional system where the meridional momentum dynamical balance is between the pressure gradient and the linear friction, like in the box model by Stommel (1961). The final equations are identical to the nonrotating 2-D equations of Marotzke *et al.* (1988), where the Fickian eddy viscosity is replaced with linear friction, and requires largely enhanced coefficients as well.

Table 1. Parameters used for the 2-D model integrations.

n_y	30	number of gridpoints in latitude
n_z	15	number of gridpoints on the vertical
H	4500 m	ocean uniform depth
W	4000 km	zonal basin extent
y_0	0 km	southern boundary position
y_1	6000 km	northern boundary position
K_H	$10^3\,\mathrm{m^2\,s^{-1}}$	horizontal tracer diffusion
K_V	$10^{-4}\,\mathrm{m^2\,s^{-1}}$	vertical tracer diffusion
g	$9.8\,\mathrm{m^2\,s^{-1}}$	gravity acceleration
f	$10^{-4}\,\mathrm{s^{-1}}$	Coriolis parameter
ρ_0	$1027\,\mathrm{kg\,m^{-3}}$	reference density
α	$2.2 \times 10^{-4}\,\mathrm{K^{-1}}$	thermal expansion coefficient
β	$7.7 \times 10^{-4}\,\mathrm{psu^{-1}}$	haline contraction coefficient
τ_T	$1.75 \times 10^{-7}\,\mathrm{s^{-1}}$	temperature restoring time
ε	$1.45 \times 10^{-4}\,\mathrm{s^{-1}}$	linear friction coefficient

These equations are solved by using a finite difference formulation (Table 1), on a uniform latitudinal grid but nonuniform vertical grid (15 levels of thickness varying from 50 m at the surface to 550 m at the bottom). No-normal-flow conditions are used on the boundaries, resulting in zero streamfunction, and zero flux conditions are applied to temperature and salinity except at the surface.

We compared all these parametrization to a full 3-D planetary geostrophic model (Huck *et al.*, 1999b), under the same forcing, i.e. restoring boundary conditions for both temperature and salinity so as to get a steady state. The linear-friction solution used afterwards is not significantly different from those employed by others (Marotzke *et al.*, 1988; Wright and Stocker, 1991), and is in good agreement with the 3-D model about thermohaline stratification and maximum overturning depth around 1000 m.

b. Surface forcing

In the next sections, the surface boundary conditions for temperature and salinity will differ ("mixed boundary conditions"), to take into account the different feedbacks on surface heat and freshwater flux. Welander (1986) took different restoring time scales for temperature and salinity. On the other hand, Weaver *et al.* (1991) used a restoring condition for surface temperature but a constant flux boundary condition for salinity; regarding variability, they concluded that the constant freshwater forcing permits decadal to centennial oscillations. Hence we follow here the latter, i.e. using constant freshwater forcing. The surface forcing is then expressed as:

$$\mathcal{F}_T = \tau_T\,[T^*(y) - \mathrm{SST}(y)], \tag{5}$$

$$\mathcal{F}_S = \frac{S_0}{h} F W, \tag{6}$$

where SST is the sea-surface temperature (uppermost model level of thickness $h = 50\,\mathrm{m}$); the restoring surface temperature and the freshwater flux read:

$$T^*(y) = 13.5\,[1 + \cos(\pi(y - y_0)/(y_1 - y_0))], \tag{7}$$

$$FW(y) = -F_0 \sin\,[2\pi(y - y_0)/(y_1 - y_0)]. \tag{8}$$

The main parameter for the following experiments is F_0; it corresponds to half of the precipitation–evaporation amplitude.

Given the positive salinity feedback on the thermohaline overturning (Marotzke, 1996), the freshwater flux forcing likely plays a key-role in the variability through increasing the meridional salinity gradient. This feedback is crucial to counterbalance the negative temperature feedback and enable the growth of an oscillatory regime.

3. Single hemisphere configuration

a. Nonlinear integrations with and without convection

This section will deal with two different experiments carried out with and without convection in order to investigate the effect of convective mixing, a very non-differentiable process, on 2-D ocean model internal variability. Different values of the freshwater forcing amplitude are determined in both cases to obtain centennial scale variability, but also to avoid millenial scale oscillations. Figure 1 shows that the two time-mean states are very similar, despite the slightly more intense overturning with no convection. Zhang *et al.* (1992) as well as Marotzke and Scott (1999) have both suggested that convective adjustment does not matter as crucially for a realistic thermohaline structure in 2-D as in 3-D since its effect remains efficiently represented through downwelling. Our two experiments show centennial variability, although it is only transient as a damped oscillation with convection, but perpetually sustained without. The effect of convection, like mixing in general, is to reduce the density gradients which are necessary to propagate the anomalies: convection mixes down any positive density anomalies on very short time scales. It is thus a sink of potential energy. However in our study aimed at understanding the variability mechanism, we will analyze both experiments with and without convection, the latter being more convenient to perform a linear stability analysis: it is likely that a qualitative study carried out with no convection would clarify the instability mechanism at the origin of oscillations growth.

The period of oscillation is deduced from the results of our nonlinear experiments, and thus the growth/damping rate ensues from the transient build-up and decay of the oscillatory regime. The convection experiment gave us a 171-yr oscillation and a 507-yr decaying time scale (Fig. 2). For the experiment without convection we find a 171-yr (coincidentally!) oscillation and a 201-yr growing time scale (Table 2). Most importantly, the density anomalies seem to be passively advected along the overturning streamlines (see Figs. 3a and 5 below).

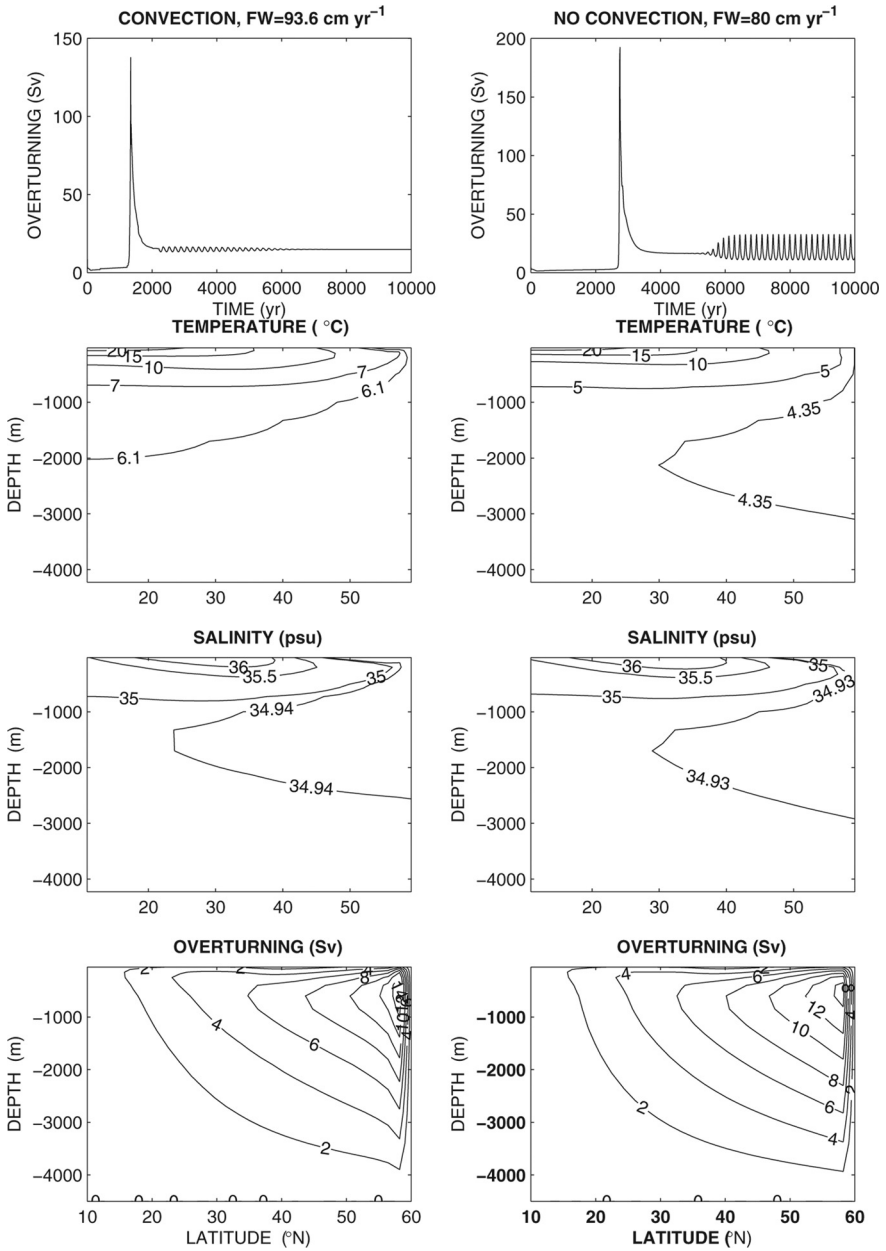

Figure 1. Two experiments with centennial variability (171 yr period for both): (left column) with convection and $FW = 93.6\,\mathrm{cm\,yr^{-1}}$; (right column) with no convection and $FW = 80\,\mathrm{cm\,yr^{-1}}$. Timeseries of the overturning streamfunction maximum; temperature, salinity and overturning averaged over the last 171 yr. The oscillations are damped in the first case, and perpetual in the second one (saturation at finite amplitude).

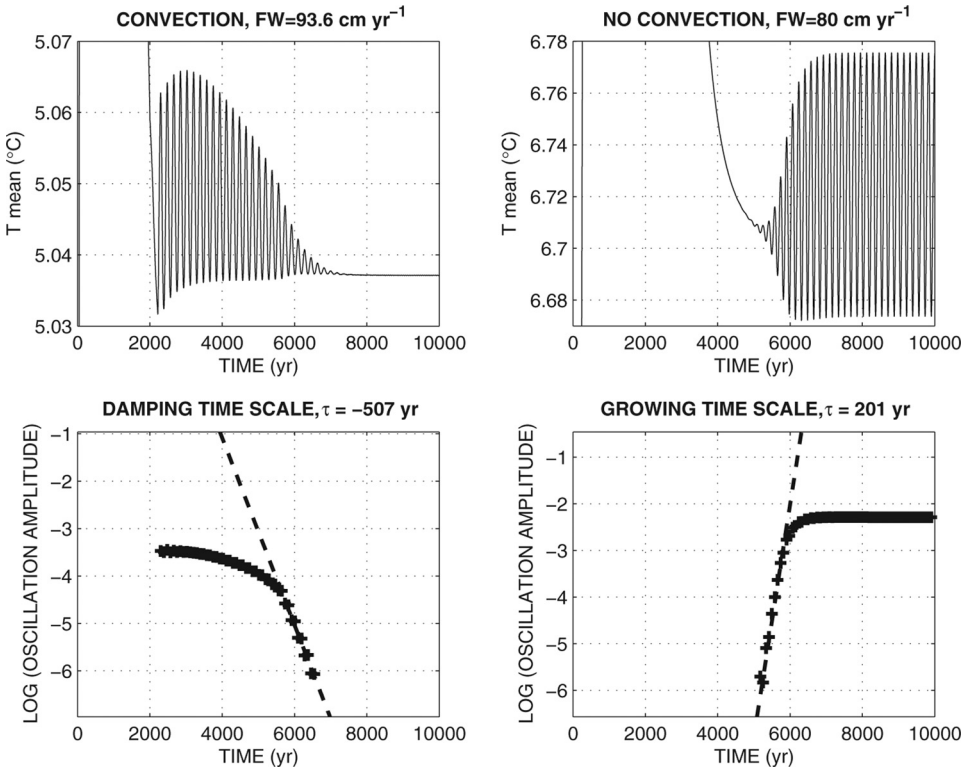

Figure 2. Time series of mean basin temperature (°C) for the two-dimensional model with convection and $FW = 93.6\,\mathrm{cm\,yr^{-1}}$ (top left), and without convection and $FW = 80\,\mathrm{cm\,yr^{-1}}$ (top right). Bottom figures show the evolution of the log of the oscillations amplitude (defined as the difference between two consecutive extremas) as a function of time, and highlight the linear behavior of the oscillations growth/decay. The damping/growing time scale is found through linear regression in the linear phase of growth/decay of oscillations.

b. Linear stability analysis

The principle of linear stability analysis is to examine the evolution of a small perturbation near a steady state. The prognostic equations of our model (3) can be written as a general dynamical system:

$$\partial_t X = \mathbf{A}(X), \tag{9}$$

where $\mathbf{A}$ is a nonlinear operator and $X = (T, S)$ is the state vector. Let $\overline{X}$ be a steady state, i.e. $\mathbf{A}(\overline{X}) = 0$, the system can be written for the perturbation $X' = X - \overline{X}$, and linearized:

$$\partial_t X' = \mathbf{M}X', \mathbf{M} = \left.\frac{\partial \mathbf{A}}{\partial X}\right|_{\overline{X}}, \tag{10}$$

where the Jacobian matrix, $\mathbf{M}$, is a function of $\overline{X}$ only (autonomous system).

Table 2. Period and growth time scale obtained from time integration (nonlinear) and predicted by the linear stability analysis (linear) of the centennial modes. These values are done for all experiments (one and two hemispheres, with and without convection/ACC) for the 2-D latitude-depth model and the Howard-Malkus loop.

One	2D with conv.		2D with no conv.		Howard-Malkus loop	
Hemisphere	nonlinear	linear	nonlinear	linear	nonlinear	linear
Period (yr)	171	424	171	162	170	167
Growth (yr)	−507	−208	201	186	454	476

Two	2D model (linear)		Howard-Malkus loop	
Hemispheres	without ACC	with ACC	nonlinear	linear
Period (yr)	733	750	605	502
Growth (yr)	−67	−129	−908	∞

A general problem for such linear stability analysis is the choice of the steady state, and that is why continuation techniques are so interesting: sometimes a steady state is readily available upon a switch of surface boundary conditions for instance (Huck and Vallis, 2001); it may also be possible, although not rigorously correct, to use the time-average of the model state over a full oscillation. In the case with convection we use the steady state reached after the decline of the oscillations near year 7000. For the case without convection, we have used the unstable steady state closest to the time-mean state over an oscillation period: we found it through an iterative solver for the zeros of the nonlinear system consisting in the time-derivatives of each gridpoint temperature and salinity (function 'fsolve' in matlab, using trust-region dogleg method), and initialized from the time-averaged temperature and salinity fields over an oscillation period.

The Jacobian matrix was calculated with two different methods; the empirical and versatile numerical method used in Huck and Vallis (2001) was found to be valid with and without convection; on the other hand, the rigorous analytical linearization of Eqs. (3) can be done only in the no-convection case. It is worth underlining that both methods gave identical results with no convection. Once the Jacobian matrix is computed for each steady state, an eigenanalysis is performed, and the oscillatory eigenmodes with largest real part are analyzed: in each case, it is a centennial scale oscillation. It is then compared to the (transient) oscillations appearing in direct integration of the nonlinear model.

In the two experiments carried out in this study, the similarities in spatial structure and time evolution are very strong between the oscillation present in the direct integration and the one issued from the most unstable linear mode. Both cases show a dipole of density anomaly is advected around the overturning circulation (Figs. 3 and 4). A phase diagram of salinity anomalies along a closed overturning streamfunction contour even shows a slowdown of the anomalies in the evaporation region, followed by a speedup in the precipitation region (Fig. 5). Furthermore, in the experiment with no convection, the oscillation period and the growth rate are very similar for the linear mode and the nonlinear model integration. However, the linear stability analysis does not provide a good quantitative estimate

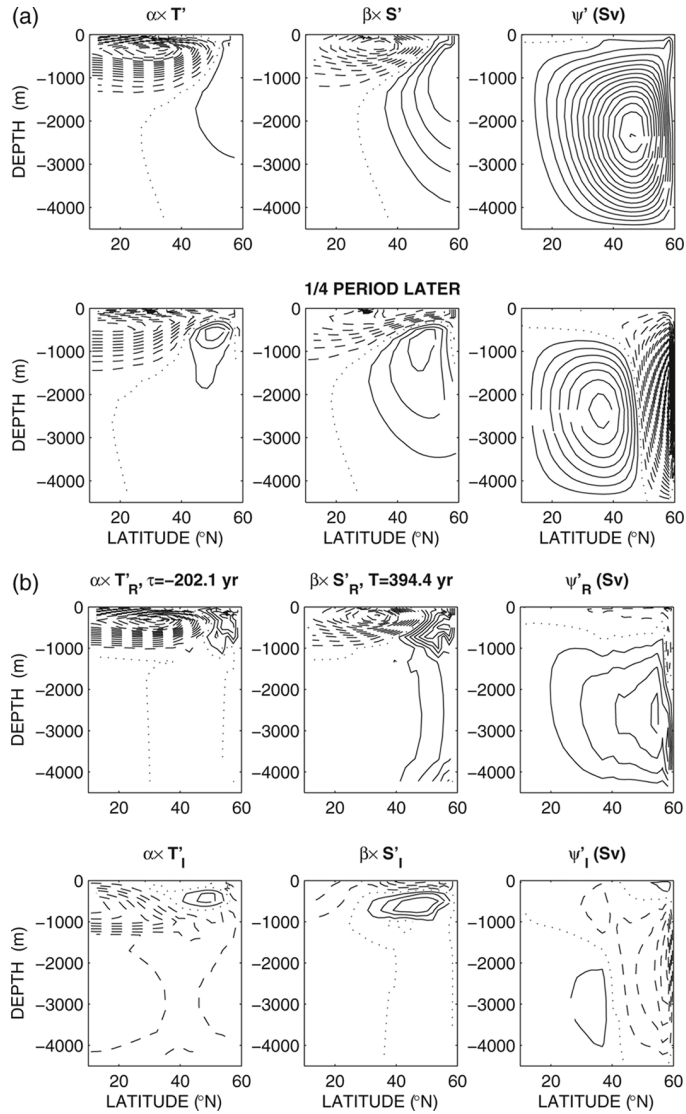

Figure 3. (a) Nonlinear model damped oscillation vs. (b) linear eigenmode (the nonlinear model year is chosen to optimize the correlation with the linear eigenvector, and the eigenvector amplitude is adjusted to give the same density variance as the nonlinear oscillation), in terms of temperature, salinity (both scaled in terms of density), and overturning anomalies, for the experiment with convection ($FW = 93.6\,\mathrm{cm\,yr^{-1}}$). (a) Snapshots are given at year 3112 and a quarter-period later. The solid, dashed and dotted lines respectively correspond to positive, negative and zero anomalies; contour interval is 2.5×10^{-6} or 0.1 Sv. (b) For the damped linear eigenmode, real and imaginary parts are provided; they evolve as: $X_R \rightarrow X_I \rightarrow -X_R \rightarrow -X_I \rightarrow X_R$, with $X = \{T', S', \psi'\}$. Spatial structure and time evolution are similar, but period (growth time scale) greatly differs: 171 (-507) vs. 424 (-208) yr.

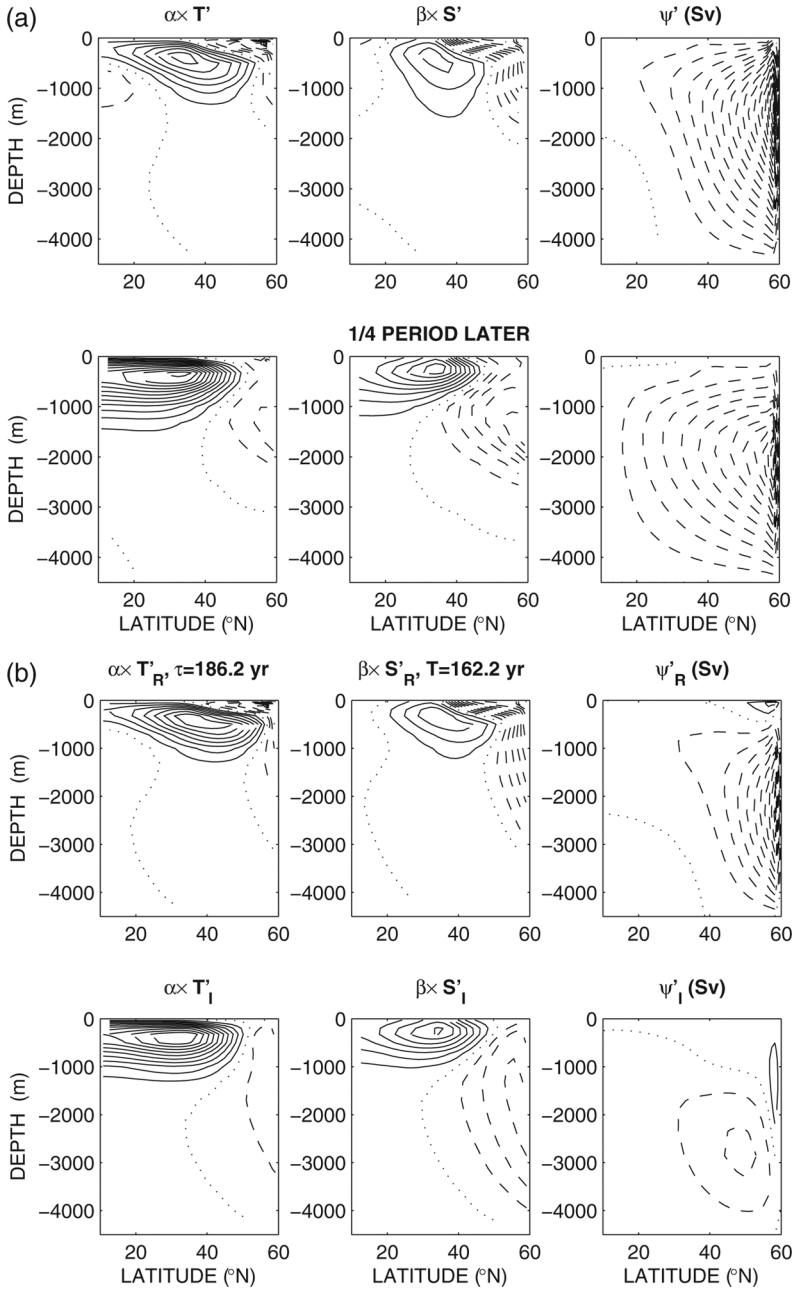

Figure 4. As in Figure 3 for the experiment with no convection ($FW = 80\,\mathrm{cm\,yr^{-1}}$): here year 9452 and a quarter-period later are shown for the sustained nonlinear oscillation, and the associated linear eigenmode is unstable; contour interval is 10^{-5} or 0.5 Sv. Note the high similarity of spatial structures and period (growing time scale): 171 (201) vs. 162 (186) yr.

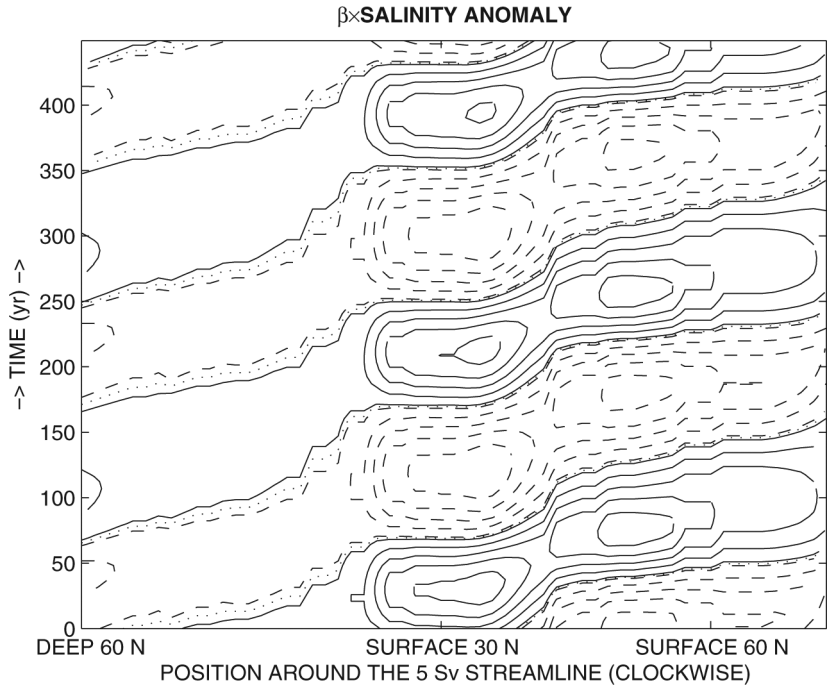

Figure 5. Hovmöller diagram of the salinity anomaly ($\times\beta$) along the 5-Sv mean streamfunction contour for the experiment with no convection (Fig. 1). The solid, dashed and dotted lines respectively correspond to positive, negative and zero anomalies. The contour interval is from 0.1 to ∞ by 6.1×10^{-2} for the positive values, and from -0.1 to $-\infty$ by -6.1×10^{-2} for the negative ones.

in the convective case (Table 2). Convection being the only nondifferentiable term, its effect on the nonlinear evolution of the perturbations is poorly assessed with this empirical linearization.

c. Density variance budget

In order to gain insight into the physical processes at the origin of oscillating perturbations, we focused on the variance budget for temperature and salinity investigated through their influence on density. Hence, further estimating the density variance budget as a simple proxy for available potential energy (Lorenz, 1955) helps in the determination of physical mechanism and spatial localization of variance sources and sinks (Arzel, 2004; Arzel *et al.*, 2006). So, in this section let us note the time average:

$$\overline{X} = \frac{1}{\mathcal{P}} \int_0^{\mathcal{P}} X \, dt, \tag{11}$$

where $\mathcal{P}$ is the oscillation period, and the anomaly is $X' = X - \overline{X}$. The domain average is then expressed as:

$$\langle X \rangle = \frac{1}{H(y_1 - y_0)} \int_{-H}^{0} \int_{y_0}^{y_1} X \, dy \, dz, \tag{12}$$

where H is the total depth, y_0 and y_1 are the domain latitude boundaries.

In the anomaly we have $\rho' = \rho_0(-\alpha T' + \beta S')$, such that:

$$\left\langle \frac{1}{2}\overline{\partial_t \rho'^2} \right\rangle = \alpha^2 \rho_0^2 \left\langle \frac{1}{2}\overline{\partial_t T'^2} \right\rangle + \beta^2 \rho_0^2 \left\langle \frac{1}{2}\overline{\partial_t S'^2} \right\rangle - \alpha\beta\rho_0^2 \, \langle \overline{\partial_t (T'S')} \rangle \, . \tag{13}$$

The density variance budget is developed hereafter from Eqs. (3) and under the following conditions: no convection, D encompasses the horizontal and vertical eddy diffusion terms, and F is the surface forcing, with the indices T and S for temperature and salinity, respectively:

$$\left\langle \frac{1}{2}\overline{\partial_t T'^2} \right\rangle = - \langle \overline{T' J(\bar{\psi}, T')} \rangle - \langle \overline{T' J(\psi', \overline{T})} \rangle + \langle \overline{D'_T T'} \rangle + \langle \overline{F'_T T'} \rangle \, , \tag{14a}$$

$$\left\langle \frac{1}{2}\overline{\partial_t S'^2} \right\rangle = - \langle \overline{S' J(\bar{\psi}, S')} \rangle - \langle \overline{S' J(\psi', \overline{S})} \rangle + \langle \overline{D'_S S'} \rangle + \langle \overline{F'_S S'} \rangle \, , \tag{14b}$$

$$\langle \overline{\partial_t (T'S')} \rangle = - \langle T' J(\bar{\psi}, S') \rangle - \langle S' J(\bar{\psi}, T') \rangle - \langle T' J(\psi', \overline{S}) \rangle - \langle S' J(\psi', \overline{T}) \rangle + \langle \overline{D'_T S'} \rangle + \langle \overline{D'_S T'} \rangle + \langle \overline{F'_T S'} \rangle + \langle \overline{F'_S T'} \rangle \, . \tag{14c}$$

Some simplifications arise from the lateral boundary conditions of zero mass, heat and salinity flux:

$$\begin{aligned} \langle \overline{T' J(\overline{\psi}, T')} \rangle &= 0, \\ \langle \overline{S' J(\overline{\psi}, S')} \rangle &= 0, \\ \langle \overline{T' J(\overline{\psi}, S')} \rangle + \langle \overline{S' J(\overline{\psi}, T')} \rangle &= 0, \\ \langle \overline{D'_T S'} \rangle &= \langle \overline{D'_S T'} \rangle \, . \end{aligned} \tag{15}$$

The last peculiarity of our variance equation derives from the constant freshwater flux:

$$\langle \overline{F'_S S'} \rangle = \langle \overline{F'_S T'} \rangle = 0. \tag{16}$$

We finally end up with the following simplified density variance budget:

$$\begin{aligned} \rho_0^{-2} \left\langle \frac{1}{2}\overline{\partial_t \rho'^2} \right\rangle = &-\alpha^2 \, \langle \overline{T' J(\psi', \overline{T})} \rangle - \beta^2 \, \langle \overline{S' J(\psi', \overline{S})} \rangle + \alpha\beta \, \langle \overline{T' J(\psi', \overline{S})} \rangle \\ &+ \alpha\beta \, \langle \overline{S' J(\psi', \overline{T})} \rangle + \alpha^2 \, \langle \overline{D'_T T'} \rangle + \beta^2 \, \langle \overline{D'_S S'} \rangle \\ &- \alpha\beta \, \langle \overline{D'_T S'} \rangle - \alpha\beta \, \langle \overline{D'_S T'} \rangle + \alpha^2 \, \langle \overline{F'_T T'} \rangle - \alpha\beta \, \langle \overline{F'_T S'} \rangle \, . \end{aligned} \tag{17}$$

Table 3. Notations for the advection, diffusion and forcing terms in the density variance budget. These terms are easily adapted to the 1-D loop model.

Advection	Diffusion	Forcing
$\mathrm{Adv}(T', \overline{T}) = \frac{-\alpha^2 \langle \overline{T' J(\psi', \overline{T})} \rangle}{\rho_0^{-2} \langle \overline{\rho'^2} \rangle}$	$\mathrm{Diff}(T', T') = \frac{\alpha^2 \langle \overline{D'_T T'} \rangle}{\rho_0^{-2} \langle \overline{\rho'^2} \rangle}$	$\mathrm{Forc}(T', T') = \frac{\alpha^2 \langle \overline{F'_T T'} \rangle}{\rho_0^{-2} \langle \overline{\rho'^2} \rangle}$
$\mathrm{Adv}(S', \overline{S}) = \frac{-\beta^2 \langle \overline{S' J(\psi', \overline{S})} \rangle}{\rho_0^{-2} \langle \overline{\rho'^2} \rangle}$	$\mathrm{Diff}(S', S') = \frac{\beta^2 \langle \overline{D'_S S'} \rangle}{\rho_0^{-2} \langle \overline{\rho'^2} \rangle}$	$\mathrm{Forc}(T', S') = \frac{-\alpha\beta \langle \overline{F'_T S'} \rangle}{\rho_0^{-2} \langle \overline{\rho'^2} \rangle}$
$\mathrm{Adv}(T', \overline{S}) = \frac{\alpha\beta \langle \overline{T' J(\psi', \overline{S})} \rangle}{\rho_0^{-2} \langle \overline{\rho'^2} \rangle}$	$\mathrm{Diff}(T', S') = \frac{-\alpha\beta \langle \overline{D'_T S'} \rangle}{\rho_0^{-2} \langle \overline{\rho'^2} \rangle}$	$\mathrm{TotForc} = \frac{-\alpha \langle \overline{F'_T \rho'} \rangle}{\rho_0^{-1} \langle \overline{\rho'^2} \rangle}$
$\mathrm{Adv}(S', \overline{T}) = \frac{\alpha\beta \langle \overline{S' J(\psi', \overline{T})} \rangle}{\rho_0^{-2} \langle \overline{\rho'^2} \rangle}$	$\mathrm{Diff}(S', T') = \frac{-\alpha\beta \langle \overline{D'_S T'} \rangle}{\rho_0^{-2} \langle \overline{\rho'^2} \rangle}$	
$\mathrm{TotAdv} = \frac{-\langle \overline{\rho' J(\psi', \overline{\rho})} \rangle}{\langle \overline{\rho'^2} \rangle}$	$\mathrm{TotDiff} = \frac{\langle \overline{D'_\rho \rho'} \rangle}{\langle \overline{\rho'^2} \rangle}$	$\mathrm{Tot} = \frac{\langle \frac{1}{2} \overline{\partial_t \rho'^2} \rangle}{\langle \overline{\rho'^2} \rangle}$

Positive and negative contributions to the tendency in density variance can be diagnosed from the numerical solutions (Tables 3 and 4). We find a balance between the anomalous streamfunction advective terms, which thus have a reduced contribution on density variance. Diffusion being a variance sink, the only source is finally the restoring surface temperature term. Moreover the spatial distribution of the total variance term (Fig. 6) shows that, although the basin average is zero, density variance sources are localized in the upper layers (0 to 500 m), mainly in the subpolar region and more weakly in the subtropics. The sinks are more important around 35N at the surface, as well as within 150 and 500 m over all latitudes, and between 750 and 2500 m close to the polar boundary.

In the surface mixed layer (thickness h_m), the correlation coefficient between temperature and salinity anomalies is more than 0.7 for both the nonlinear integration and the linear eigenvector, it allows us write approximately that in the mixed layer $S' = rT'$. Then, the variance term associated with surface restoring temperature reads:

$$\begin{aligned} -\alpha\rho_0^{-1} \langle \overline{F'_T \rho'} \rangle &= \alpha^2 \langle \overline{F'_T T'} \rangle - \alpha\beta \langle \overline{F'_T S'} \rangle \\ &= \langle \left(\overline{-\alpha^2 \tau_T T'^2 + \alpha\beta \tau_T T' S'} \right) H(z + h_m) \rangle \\ &= \langle \left(\overline{-\alpha^2 \tau_T T'^2 + \alpha\beta \tau_T r T'^2} \right) H(z + h_m) \rangle \\ &= \langle \left(\overline{(\beta r - \alpha) \alpha \tau_T T'^2} \right) H(z + h_m) \rangle , \end{aligned} \tag{18}$$

where H is the Heaviside function. It clearly appears that this type of forcing becomes a source of variance when:

$$-\alpha\rho_0^{-1} \langle \overline{F'_T \rho'} \rangle > 0 \Rightarrow r > \frac{\alpha}{\beta}. \tag{19}$$

Table 4. Source (positive) and sink (negative) terms in the density variance budget (yr^{-1}) for the nonlinear model oscillation and for the linear eigenmode (whose phase is fitted to optimize the correlation with nonlinear model oscillation, and amplitude is adjusted to give the same density variance). The analysis is performed for the single hemispheric latitude-depth model (nonlinear case, corresponding to direct integration, and linear one, corresponding to the eigenmode of the linear stability analysis) and for the Howard-Malkus loop (with two different values of r_T).

One hemisphere:	Latitute-depth model		Howard-Malkus loop	
Variance term	nonlinear	linear	$r_T = 1\,\mathrm{yr}^{-1}$	$r_T = 0.1\,\mathrm{yr}^{-1}$
$\mathrm{Adv}(T', \overline{T})$	0.148	−0.018	0.00076	0.00377
$\mathrm{Adv}(S', \overline{S})$	0.0584	−0.003	0.00226	0.00198
$\mathrm{Adv}(T', \overline{S})$	−0.062	0.007	−0.00003	−0.00033
$\mathrm{Adv}(S', \overline{T})$	−0.144	0.017	−0.00052	−0.00488
TotAdv	**0.000**	**0.004**	**0.00247**	**0.00054**
$\mathrm{Diff}(T', T')$	−0.123	−0.137	0.00000	−0.00008
$\mathrm{Diff}(S', S')$	−0.059	−0.061	−0.00228	−0.00242
$\mathrm{Diff}(T', S')$	0.056	0.063	0.00000	0.00010
$\mathrm{Diff}(S', T')$	0.056	0.063	0.00000	0.00010
TotDiff	**−0.070**	**−0.072**	**−0.00228**	**−0.00230**
$\mathrm{Forc}(T', T')$	−0.026	−0.029	−0.00076	−0.00371
$\mathrm{Forc}(T', S')$	0.096	0.095	0.00066	0.00464
TotForc	**0.070**	**0.065**	**−0.00010**	**0.00093**
Tot	**0.000**	**−0.003**	**0.00009**	**−0.00083**

Table 5. Parameters used for the Howard-Malkus loop model.

α	$2.2 \times 10^{-4}\,\mathrm{K}^{-1}$	thermal expansion coefficient
β	$7.7 \times 10^{-4}\,\mathrm{psu}^{-1}$	haline contraction coefficient
k	$34.4\,\mathrm{yr}^{-1}$	buoyancy torque/overturning parameter
r_T	$1\,\mathrm{yr}^{-1}$	temperature restoring time
T_0	10 K	temperature forcing amplitude
h	1000 m	fluid thickness
S_0	35 psu	reference salinity
F_0	$80/101\,\mathrm{cm\,yr}^{-1}$	freshwater flux intensity (1 hemisphere/2 hemisphere)
K_ϕ	$2.2 \times 10^{-3}\,\mathrm{yr}^{-1}$	tracer diffusion
$I^T(\phi)$	$-\sin(\phi)$	temperature forcing geometry in one-hemisphere
	$\cos(2\phi)\Pi_{\left[\frac{\pi}{2}, \frac{3\pi}{2}\right]}$	temperature forcing geometry in two-hemisphere
$I^S(\phi)$	$-\sin(2\phi)\Pi_{\left[\frac{\pi}{2}, \frac{3\pi}{2}\right]}$	salinity forcing geometry in one-hemisphere
	$\sin(4\phi)\left(\Pi_{\left[\frac{\pi}{2}, \pi\right]} - \Pi_{\left[\pi, \frac{3\pi}{2}\right]}\right)$	salinity forcing geometry in two-hemisphere

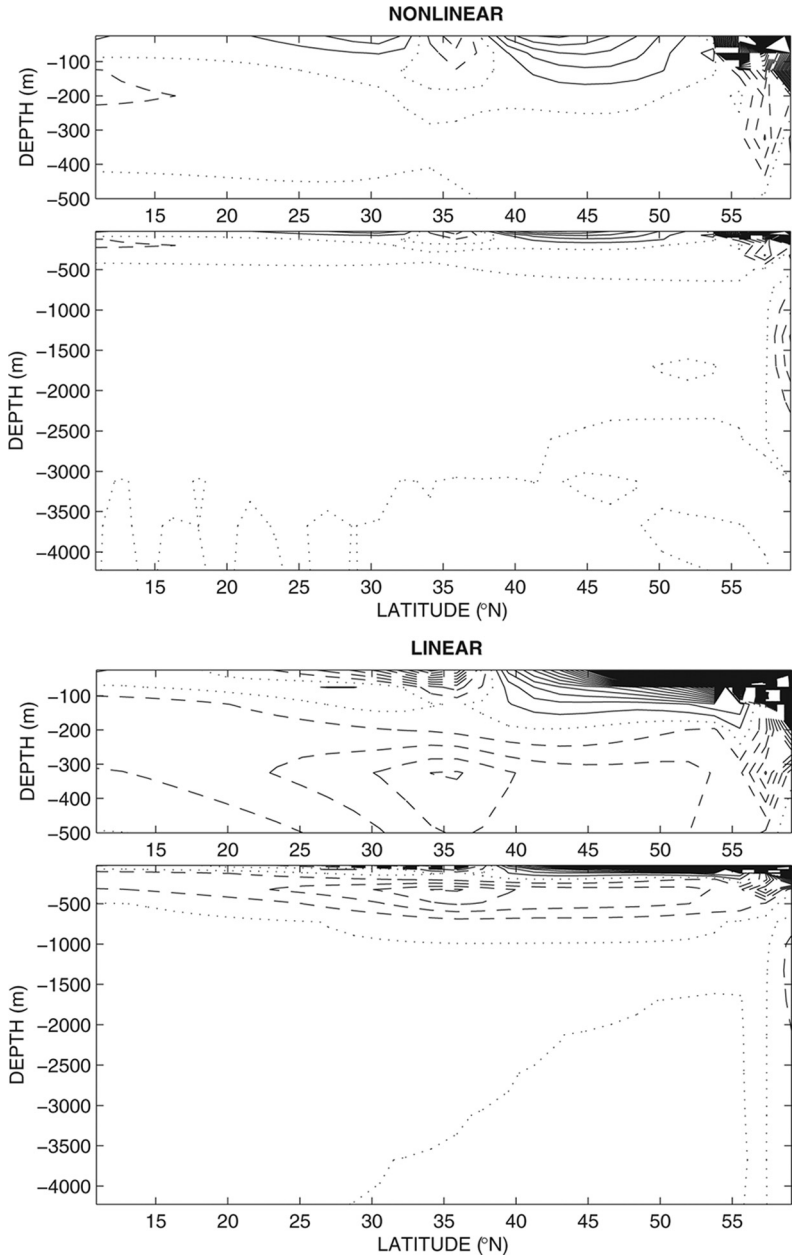

Figure 6. Spatial distribution of the total density variance term $\frac{1}{2}\overline{\partial_t \rho'^2} / \langle \overline{\rho'^2} \rangle$, for the nonlinear model integration with no convection, averaged over an oscillation period and for the associated linear oscillatory eigenmode. The solid, dashed and dotted lines respectively correspond to the positive, negative and zero variances, the contour interval is $0.2\,\mathrm{yr}^{-1}$. Both nonlinear and linear modes give similar qualitative results.

A linear regression gives $r = 1.06\,\text{psu K}^{-1}$ for the nonlinear integration and $r = 0.91\,\text{psu K}^{-1}$ for the eigenvectors; these values should be compared to $\alpha/\beta = 0.29\,\text{psu K}^{-1}$. Thus the condition (19) is fulfilled and allows the surface temperature relaxation to generate density variance.

In conclusion, under mixed boundary conditions, the surface temperature restoring forcing provides a source of density variance sustaining the variability: this ensues from the good correlation between temperature and salinity anomalies at the surface during oscillations. When positive (negative) density anomalies consisting of positive (negative) anomalies of temperature and salinity are exposed to surface forcing, the relaxation to zero of the temperature anomaly induces the intensification of the density anomaly. It is worth noting that similar conclusions have been drawn about interdecadal oscillations under mixed boundary conditions (Arzel, 2004; Arzel *et al.*, 2006).

We are thus led to consider the cause of such positive correlations between temperature and salinity anomalies. Given the mean $\theta - S$ relationship in the ocean, and the correspondence between regions of warming (cooling) and evaporation (precipitation), variations in the circulation induce $T - S$ anomalies with positive correlations, just like the mean $T - S$ relationship. Alternatively, perturbation structures, whose density is dominated by salinity, but without such a good correlation between $T - S$ anomalies would not be able to draw energy from the surface forcing, and hence would not appear as weakly unstable or damped modes, but much further in the eigenvalue spectrum.

4. A minimal model: The Howard-Malkus loop oscillator

The 2-D model oscillation shows advection of temperature and salinity anomalies along contours of the mean overturning streamfunction (Fig. 5). To simplify the system further, it seems appropriate to model our basin as the Howard-Malkus loop (Malkus, 1972), a 1-D model of the overturning circulation. This widely studied oscillator (Welander, 1957, 1965; Keller, 1966; Welander, 1967, 1986; Winton and Sarachik, 1993; Dewar and Huang, 1995, 1996; Huang and Dewar, 1996) is composed of a fluid contained in a circular loop (Fig. 7). The uniform angular velocity ω is proportional to the buoyancy torque integrated around the loop (Maas, 1994) through a dynamical balance between the buoyancy forces and the friction as done in the Stommel (1961) box model. As shown above, we set mixed boundary conditions, i.e. prescribed freshwater (salinity) flux and temperature restoring (the forcing distribution along the loop is not necessarily restricted to the 'surface'). The evolution equations for temperature and salinity in this fluid loop read:

$$\partial_t T + \omega \partial_\phi T = r_T [T_0 I^T(\phi) - T] + K_\phi \partial_\phi^2 T, \tag{20a}$$

$$\partial_t S + \omega \partial_\phi S = -\frac{F_0 S_0}{h} I^S(\phi) + K_\phi \partial_\phi^2 S, \tag{20b}$$

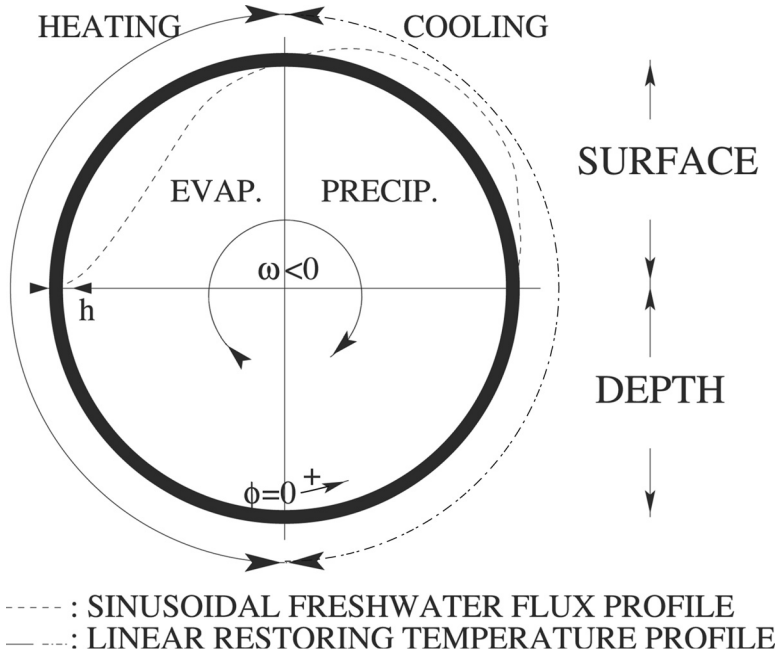

Figure 7. Schematic of the Howard-Malkus loop oscillator along with the temperature and freshwater (dashed) forcing profiles used here.

where ω is the overturning pulsation and is given by

$$\omega = -k \int_0^{2\pi} (-\alpha T + \beta S) \sin\phi \, d\phi, \tag{21}$$

where T is the temperature, S is the salinity, α is the thermal expansion coefficient, β is the haline contraction coefficient, ϕ is the counterclockwise angle around the loop measured from the bottom, F_0 is the freshwater flux intensity, S_0 is the reference salinity, h is the fluid thickness, r_T is the relaxation coefficient for temperature (inverse of the restoring time), T_0 is the amplitude of the temperature forcing, $I^{\{T,S\}}$ is the temperature and salinity forcing geometry, and K_ϕ is a Laplacian eddy diffusion used for the numerical integration only. The proportionality factor k between the overturning and the buoyancy torque is such that it gives a realistic overturning value for typical temperature and salinity contrasts. One should note the lack of convection, here, resulting from the absence of difference between horizontal and vertical processes.

a. Nonlinear integrations and density variance budget

First we verify that the Malkus loop oscillator is a valid approximation to represent our 2-D oscillation. The numerical integration of the Malkus loop equations with the parameters

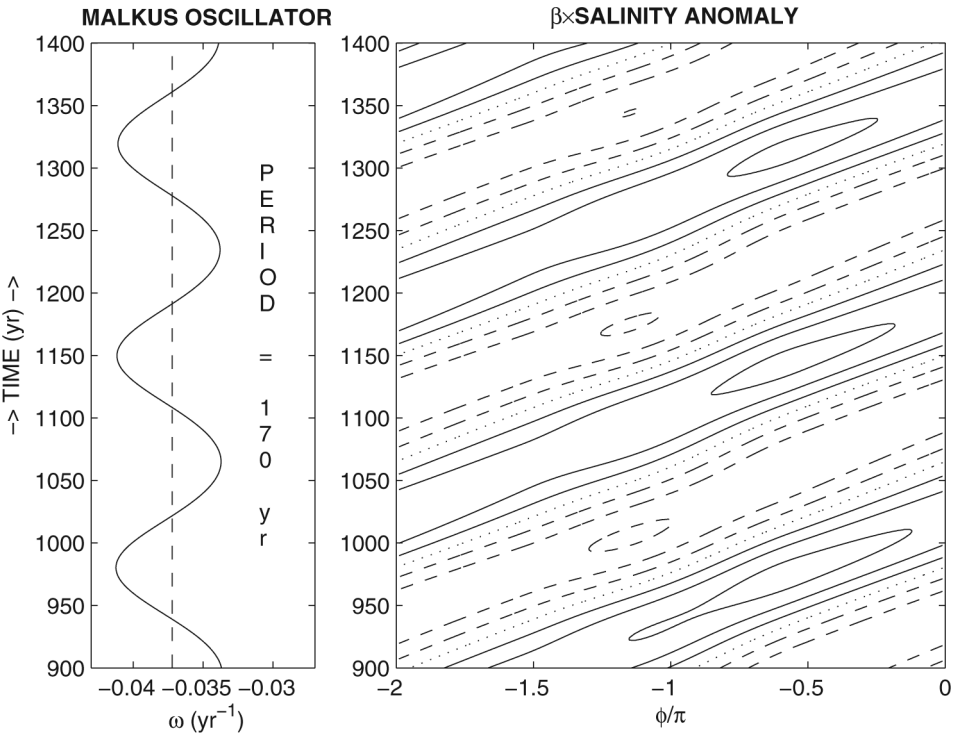

Figure 8. Numerical integration of the nonlinear Malkus loop oscillator leading to perpetual oscillations. (left) Overturning as a function of time. (right) Hovmöller diagram of the salinity anomaly ($\times\beta$). The solid, dashed and dotted lines respectively correspond to positive, negative and zero anomalies, the contour interval is 0.75×10^{-4}. The oscillation period is 170 yr for an advective period $2\pi/\overline{\omega} = 169$ yr and the propagation is governed by the advection of the mean overturning circulation.

given in Table 5 settles into perpetual oscillations (note the small diffusion term added for numerical stability). The friction parameter k was adjusted in order to get a mean overturning period ($2\pi/\overline{\omega}$, where $\overline{\omega}$ is the time-averaged ω) equal to the renewal time of the water from the two-dimensional model (basin volume/maximum overturning $\sim$ 171 yr).

In the nonlinear integration with perpetual oscillations, the diffusion and nonlinear term finally balance the initial (linear) growth of the perturbation. The oscillation period (Fig. 8) is 170 yr vs. 171 yr in the 2-D model, as a consequence of the choice for parameter k. Salinity anomalies clearly propagate at the angular velocity of the time-averaged overturning (Fig. 8 to be compared to Fig. 5 for the 2-D model). Temperature (salinity) anomalies are about 0.09°C (0.70 psu), and thus density anomalies are dominated by salinity. These two results suggest that oscillations in the 2-D model and the Malkus loop oscillator are governed by the same physical processes (in the next section we will provide a quasi-analytical stability analysis of the loop oscillator in order to characterize the oscillation mechanism).

In order to compare the oscillations in this very simple model to those in the 2-D one, a similar density variance budget is performed (Table 4). It shows that, for standard coefficients, there is no need to have a positive surface temperature relaxation term for sustaining the oscillations. Hence, the surface relaxation may not be fundamental to the oscillatory mechanism. In fact, here, the contribution by the advective terms to the variance budget is positive.

A second simulation conducted with a reduced relaxation coefficient ($r_T = 0.1\,\mathrm{yr}^{-1}$) allowed us to explore a parameter regime more similar to the one used in the 2-D experiments: indeed the density variance terms now compare much better to the 2-D case, with a positive contribution of surface temperature relaxation.

From these two simulations, the density variance budget suggests that, at least for the Howard Malkus loop, the fundamental contributor to the growth of the centennial oscillation is not the surface relaxation. However, the temperature relaxation remains a necessary element for this growth: indeed, we performed the same simulations with prescribed heat fluxes diagnosed as the time-averaged temperature restoring term over one oscillation period, and observed as expected the decay of oscillations. The growth of oscillations occurs only on condition (i) that the density be affected by both temperature and salinity and (ii) that the restoring time scale associated to T and S be different; thus, the mean circulation is controlled by the more rapidly relaxed variable (temperature here) whereas the oscillations rely on the more 'free' variable (salinity) that is not restored.

b. Linear stability analysis

The periodicity of the Malkus loop suggests that the spectrum of the solutions is discontinuous in terms of ϕ and allows the following decomposition:

$$X(t) = \Re\left[\sum_{n\epsilon N} X_n(t) e^{in\phi}\right],$$

where $\Re$ indicates the real part, with the reverse projection:

$$X_n = X_{rn} + iX_{in} = \frac{1}{2\pi}\int_0^{2\pi} X e^{-in\phi} d\phi,$$

where X represents T or S. The inviscid Malkus oscillator equations can thus be rewritten as:

$$\partial_t S_{rn} - n\omega S_{in} = -\frac{F_0 S_0 I^S_{rn}}{h}, \tag{22a}$$

$$\partial_t S_{in} + n\omega S_{rn} = -\frac{F_0 S_0 I^S_{in}}{h}, \tag{22b}$$

$$\partial_t T_{rn} - n\omega T_{in} = r_T(T_0 I^T_{rn} - T_{rn}), \tag{22c}$$

$$\partial_t T_{in} + n\omega T_{rn} = r_T(T_0 I^T_{in} - T_{in}), \tag{22d}$$

where the subscripts r and i respectively state for the real and imaginary parts and $I_n^{\{T,S\}}$ respectively represent the specific geometry of the temperature and salinity forcing:

$$I_n^{\{T,S\}} = I_{rn}^{\{T,S\}} + i\, I_{in}^{\{T,S\}} = \frac{1}{2\pi}\int_0^{2\pi} I^{\{T,S\}}(\phi) e^{-in\phi} d\phi.$$

It appears that ω depends only on the first harmonic in T and S:

$$\omega = -k\alpha T_{i1} + k\beta S_{i1}. \tag{23}$$

The steady state ($\partial_t \equiv 0$) reads in terms of ω:

$$\overline{S}_{rn} = -\frac{F_0 S_0 I_{in}^S}{n\overline{\omega} h}, \tag{24a}$$

$$\overline{S}_{in} = \frac{F_0 S_0 I_{rn}^S}{n\overline{\omega} h}, \tag{24b}$$

$$\overline{T}_{rn} = \frac{r_T^2 T_0 I_{rn}^T + n\overline{\omega} r_T T_0 I_{in}^T}{r_T^2 + n^2\overline{\omega}^2}, \tag{24c}$$

$$\overline{T}_{in} = \frac{r_T^2 T_0 I_{in}^T - n\overline{\omega} r_T T_0 I_{rn}^T}{r_T^2 + n^2\overline{\omega}^2}. \tag{24d}$$

Introducing these expressions in (23) gives a fourth-order equation for the steady-state overturning:

$$\overline{\omega}^4 + \left(r_T^2 - \frac{k\beta F_0 S_0 I_{r1}^S}{h} - k\alpha r_T T_0 I_{r1}^T\right)\overline{\omega}^2 + k\alpha r_T^2 T_0 I_{i1}^T \overline{\omega} - r_T^2 \frac{k\beta F_0 S_0 I_{r1}^S}{h} = 0. \tag{25}$$

The linear stability analysis around the steady state is performed using the standard notations:

$$\{T, S\}_{\{r,i\}n} = \{\overline{T}, \overline{S}\}_{\{r,i\}n} + \{T', S'\}_{\{r,i\}n},$$

where the overbar and the prime indicate the steady state value and the perturbation, respectively. Linearization leads to:

$$\partial_t \begin{pmatrix} S'_{rn} \\ S'_{in} \\ T'_{rn} \\ T'_{in} \end{pmatrix} = \begin{pmatrix} 0 & n\overline{\omega} + nk\beta\overline{S}_{in}\delta_{1,n} & 0 & -nk\alpha\overline{S}_{in}\delta_{1,n} \\ -n\overline{\omega} & -nk\beta\overline{S}_{rn}\delta_{1,n} & 0 & nk\alpha\overline{S}_{rn}\delta_{1,n} \\ 0 & nk\beta\overline{T}_{in}\delta_{1,n} & -r_T & n\overline{\omega} - nk\alpha\overline{T}_{in}\delta_{1,n} \\ 0 & -nk\beta\overline{T}_{rn}\delta_{1,n} & -n\overline{\omega} & -r_T + nk\alpha\overline{T}_{rn}\delta_{1,n} \end{pmatrix} \begin{pmatrix} S'_{rn} \\ S'_{in} \\ T'_{rn} \\ T'_{in} \end{pmatrix}, \tag{26}$$

where δ is the Kronecker symbol. The diagonalization of the Jacobian matrix provides the eigenvectors and their associated eigenvalues.

Now, we will distinguish the case $n = 1$ from the one where $n \neq 1$ in our analysis. If $n \neq 1$ four complex eigenvalues are obtained:

$$\lambda_{n1\pm} = \pm in|\overline{\omega}|, \tag{27a}$$

$$\lambda_{n2\pm} = -r_T \pm in|\overline{\omega}|. \tag{27b}$$

They correspond to the subharmonics of ω; one of them is a damped oscillation due to temperature restoring. The case where $n = 1$ is more interesting because the overturning anomalies are included. This is why focus, hereafter, will be on it; the index will be dropped accordingly for simplification of notations. It is worth recalling that the $n = 1$ projection completely describes the advection term ω.

Figure 9 shows the stability diagram as a function of the freshwater intensity F_0, keeping the other values alike those given in Table 5. The steady state is unstable when $F_0 > 0$, and the most unstable eigenmode is oscillatory for $F_0 < 1470\,\mathrm{cm\,yr^{-1}}$ for $1/r_T = 1$ yr (the fixed point is an unstable spiral). Above this threshold the fixed points become unstable nodes, but their unstable modes are not oscillatory. All the eigenvectors are more marked in salinity than in temperature, and thus the associated density anomaly ($\beta|S'_{\{r,i\}}| \gg \alpha|T'_{\{r,i\}}|$).

Negligible variations of temperature allow us to step further in the simplification process and to consider the overturning variations only controlled by salinity anomalies: the linear subsystem is then easily expressed analytically. Hereafter we will consider two cases according to the salinity conditions: (i) with a passive salinity (advected by a mean overturning), and (ii) with active salinity and passive temperature.

i. Fixed temperature and fixed overturning ($\partial_{\rho'}\omega = 0$). By prescribing both the temperature and the angular velocity, (26) becomes:

$$\partial_t \begin{pmatrix} S'_r \\ S'_i \end{pmatrix} = \begin{pmatrix} 0 & -\overline{\omega} \\ \overline{\omega} & 0 \end{pmatrix} \begin{pmatrix} S'_r \\ S'_i \end{pmatrix}, \tag{28}$$

and the eigenvalues are simply: $\lambda_\pm = \pm i|\overline{\omega}|$. The first subharmonic is thus equivalent to those in the $n \neq 1$ case. The approximation of fixed ω comes to neglect the projection of the first harmonic perturbations ($n = 1$), then it is logical to find the same type of solution as for $n \neq 1$.

ii. Salinity-controlled overturning. Here, the influence of temperature anomalies on the overturning is assumed to be negligible compared to the effect of salinity anomalies. Then (26) becomes

$$\partial_t \begin{pmatrix} S'_r \\ S'_i \\ T'_r \\ T'_i \end{pmatrix} = \begin{pmatrix} 0 & \overline{\omega} + k\beta\overline{S}_i & 0 & 0 \\ -\overline{\omega} & -k\beta\overline{S}_r & 0 & 0 \\ 0 & k\beta\overline{T}_i & -r_T & \overline{\omega} \\ 0 & -k\beta\overline{T}_r & -\overline{\omega} & -r_T \end{pmatrix} \begin{pmatrix} S'_r \\ S'_i \\ T'_r \\ T'_i \end{pmatrix}. \tag{29}$$

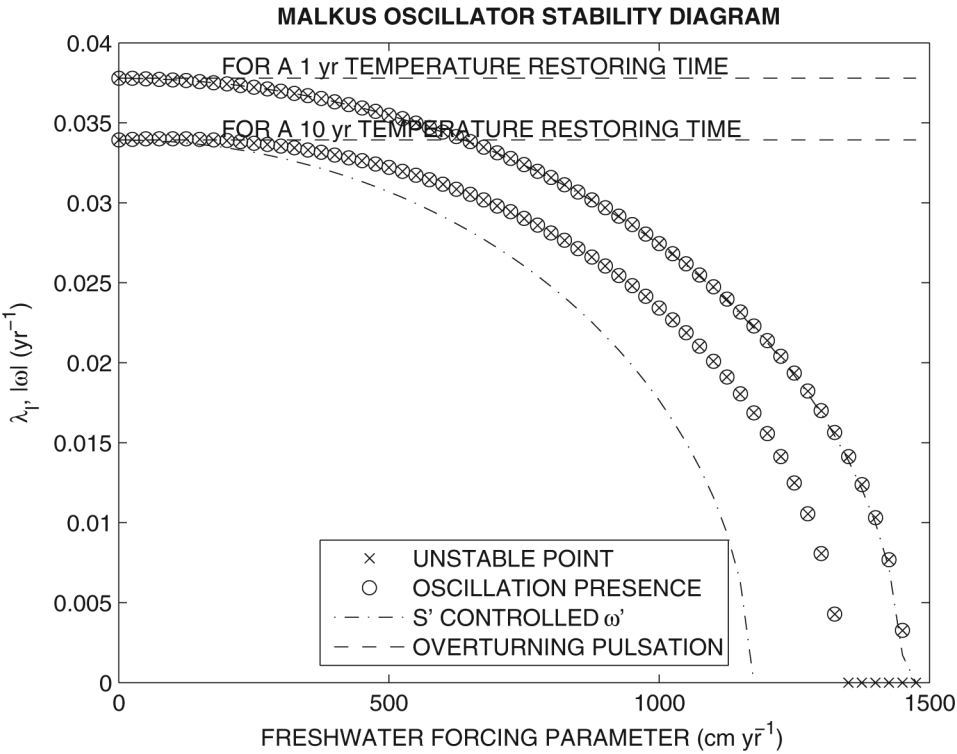

Figure 9. Stability diagram of the Malkus loop oscillator as a function of the freshwater intensity F_0 (up to very strong, unrealistic, values). Ordinate is the imaginary part of the eigenvalues for our different approximated systems compared to the overturning pulsation (dashed). All the points are unstable (except for $F_0 = 0$). The largest real part eigenmode is oscillatory until the critical values $F_0 = 1470$ (1350) cm yr^{-1} for the 1-yr (10-yr) temperature restoring time. Horizontal lines are the steady-state overturning pulsation in each case. The 'salinity-controlled overturning' subsystem is plotted in dash-dotted line.

In addition, we impose a realistic salinity forcing $I^S(\phi)$, consisting in an antisymmetric meridional structure (implying $I_r^S = 0$, see Fig. 7). The steady salinity structure is now symmetric ($\overline{S_i} = 0$). Using the steady state values (24c-d), the eigenvalues then satisfy

$$\left[\lambda^2 - \frac{k\beta F_0 S_0 I_i^S}{h\overline{\omega}}\lambda + \overline{\omega}^2\right][(\lambda + r_T)^2 + \overline{\omega}^2] = 0. \tag{30}$$

Let us focus first on the second part of this equation: the solutions of $(\lambda + r_T)^2 + \overline{\omega}^2 = 0$ are the complex conjugates $-r_T \pm i|\overline{\omega}|$. It corresponds to an oscillation at the overturning period with a strong damping rate $O(1\,\text{yr})$.

For the other part of the eigenvalues equation: $\lambda^2 - \lambda(k\beta F_0 S_0 I_i^S)/(h\overline{\omega}) + \overline{\omega}^2 = 0$, oscillations are possible only if

$$F_0 < \frac{2h\overline{\omega}^2}{k\beta S_0 |I_i^S|}. \tag{31}$$

Using the parameters in Table 5, the criterion becomes $F_0 < 1372\,\mathrm{cm\,yr^{-1}}$ and applies fairly well to the general system too (Fig. 9), especially whenever the temperature restoring time is shortened. Eq. (31) can be interpreted as a nondimensional ratio between freshwater forcing and overturning advection: Increase of F_0 decreases the characteristic freshwater time scale, which becomes more important than the advection over the time evolution of the anomalies, and eventually disables the advective oscillation.

If the oscillation criterion is satisfied we get $\lambda = \lambda_r + i\lambda_i$, with

$$\lambda_i = |\overline{\omega}| \sqrt{1 - \left(\frac{k\beta F_0 S_0 I_i^S}{2h\overline{\omega}^2} \right)^2}. \tag{32}$$

Given (31), $0 < \lambda_i < \overline{\omega}$, i.e. the oscillation period is systematically longer than the average overturning period. The oscillation growth rate is

$$\lambda_r = \frac{k\beta F_0 S_0 I_i^S}{2h\overline{\omega}} > 0, \tag{33}$$

which is always positive for our parameters (thermally-driven $\overline{\omega} < 0$, and $I_i^S < 0$ for tropical evaporation and subpolar precipitation): thus the oscillations are unstable. If (31) is satisfied the fixed point is an unstable spiral, otherwise it is an unstable node.

c. Physical mechanism of the oscillations

i. How can one understand the growth of the perturbations? Let us consider a positive haline anomaly at the equator surface advected by a thermal circulation ($\omega < 0$, Fig. 10a). This anomaly reduces the meridional density gradient, and thus the resulting buoyancy torque reduces the overturning circulation. The residence time in the evaporation zone is then increased, which strengthens the anomaly. Then, when the anomaly quits the evaporation zone to enter the precipitation zone, it increases the meridional density gradient, and the overturning circulation is now enhanced by the resulting buoyancy torque. The residence time in the precipitation zone is then decreased. Since the positive haline anomaly spends more time in the evaporation zone than in the precipitation zone, it experiences a net salt increase. A same argument is valid for a negative haline anomaly. These sketches were numerically confirmed by introducing salinity perturbations in the loop model with weak diffusion and by following their evolution with time. It is worth noting that the growth crucially depends on the fact that the buoyancy flux resulting from the freshwater forcing opposes the buoyancy forcing resulting from the thermal fluxes, which set the sign of the overturning circulation. If the fluxes were not opposed, they would damp any anomaly (Fig. 10b).

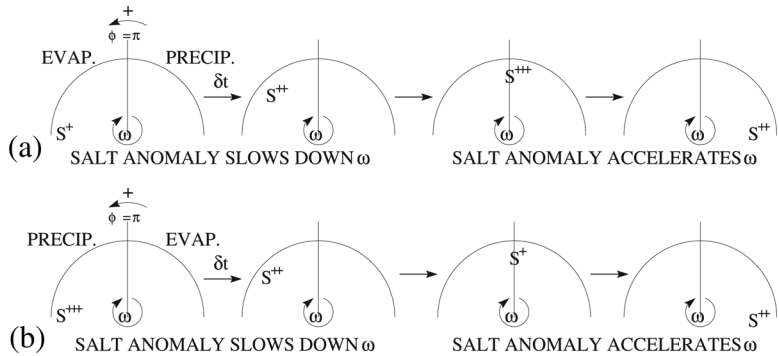

Figure 10. Schematic representation of the time evolution of salinity anomalies passing through the freshwater forcing zone and influencing the overturning ω. Growth or decay perturbation is a function of the freshwater forcing configuration: (a) tropical evaporation and subpolar precipitation lead to perturbation growth, whereas (b) tropical precipitation and subpolar evaporation lead to perturbation decay.

ii. How can one understand the oscillation? Let us imagine an initial dipole salinity perturbation (which is the one with the main projection on the overturning), the positive perturbation is in the equatorial region and the negative one in the polar region ($S_i' > 0$). The circulation, which is prescribed by the buoyancy torque, is thus reduced ($\omega' > 0$, recall $\overline{\omega} < 0$). Because in this parameter regime the perturbed salt advection term is dominated by the advection by the mean flow (as will be discussed in the following paragraph), the advection of the dipole perturbation moves the positive perturbation to the top of the loop and the negative one to the bottom ($S_r' < 0$, and $\omega' = 0$). The dipole keeps being advected clockwise and the negative perturbation comes into the polar region while the positive one enters the equatorial region ($S_i' < 0$, $\omega' < 0$). Next the mean advection leads the positive pertubation into the bottom region and the negative one in the top region ($S_r' > 0$, $\omega' = 0$). Then the positive perturbation moves to the equatorial region and the negative one to the polar region: we are back to the initial perturbation ($S_i' > 0$, $\omega' > 0$), and the oscillation cycle can repeat itself indefinitely. This simple advective mechanism is illustrated in Figure 11.

iii. What is the connection between this salinity oscillation mechanism and the more traditional positive salinity feedback? We can define a nondimensional parameter controlling the salinity oscillation regime or the salinity feedback regime according to (31):

$$\frac{2h\bar{\omega}^2}{k\beta F_0 S_0 |I_i^S|} = \frac{\tau_{SF}^2}{\tau_O^2}. \tag{34}$$

The characteristic response time of the overturning to the salinity forcing is defined as:

$$\tau_{SF} = \sqrt{\frac{2h}{k\beta F_0 S_0 |I_i^S|}}.$$

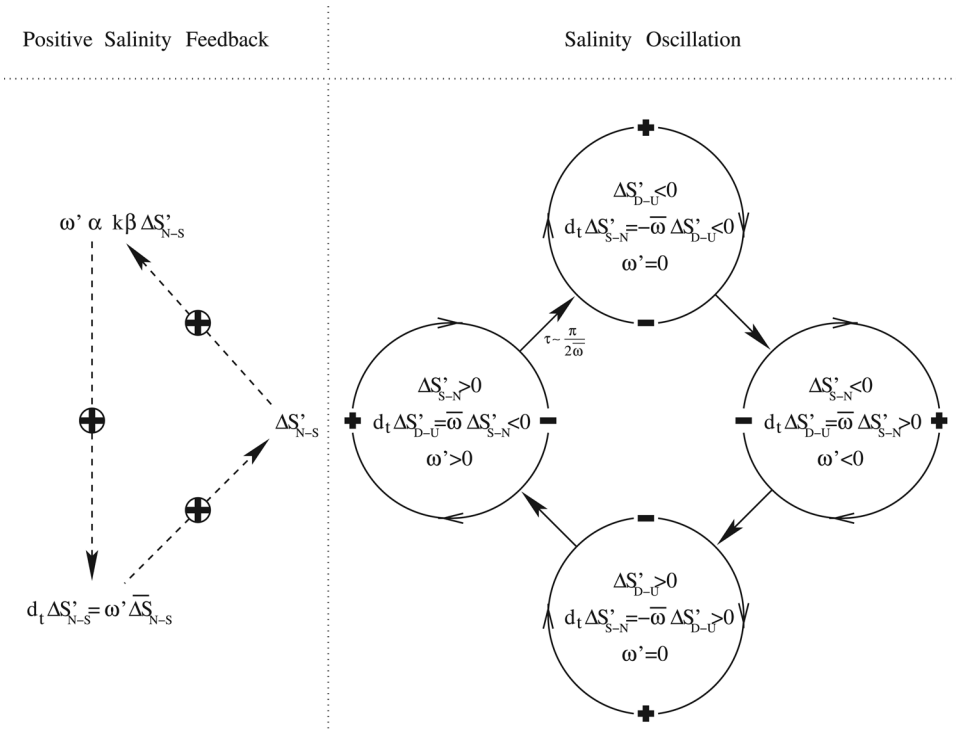

Figure 11. Schematic representation of the different mechanisms between the salinity oscillation regime (right, solid arrows) and the positive salinity feedback (left, dashed arrows). South-North (Down-Up) salinity gradients, $\Delta S'_{S-N}$ ($\Delta S'_{D-U}$), correspond to S'_i (S'_r) in the Howard-Malkus loop. Whether $\overline{\omega}\partial_\phi S'$ or $\omega'\partial_\phi \overline{S}$ term dominates the perturbed salinity advection we obtain respectively the salinity oscillation or the positive salinity feedback: (left) a retroaction diagram is sketched, arrows with circled signs corresponding to the sign of coupling; (right) the phases of a salinity oscillation are sketched, the circle represents the overturning loop ($\overline{\omega} < 0$), the $\pm$ signs corresponding to the sign of salinity anomalies, and the arrows corresponds to about a quarter-period delayed response. In some cases, oscillations will be sustained, at second order, by the positive salinity feedback.

This derives from the rate of change of the overturning (21) as a function of the salinity meridional gradient ($k\beta$), through the influence of the salinity surface forcing only in (20b): $F_0 S_0 |I_i^S|/h$. The characteristic time of the overturning circulation is simply:

$$\tau_O = \frac{1}{|\overline{\omega}|}.$$

A comparison of the two advection terms for the evolution of salinity anomaly, i.e. the mean flow advection of the salinity perturbation gradient and the anomalous advection of

the mean salinity gradient, shows a strong relation with these two timescales:

$$\frac{O(\overline{\omega}\partial_\phi S')}{O(\omega'\partial_\phi \overline{S})} = \frac{O\left(\overline{\omega}\sqrt{S_i'^2 + S_r'^2}\right)}{O(k\beta S_i'|\overline{S_r}|)} \approx \frac{\overline{\omega}^2 h}{k\beta F_0 S_0 |I_i^S|} \approx \frac{1}{2}\frac{\tau_{SF}^2}{\tau_O^2}. \tag{35}$$

Two cases arise depending on the ratio of these two characteristic times:

- If $\tau_{SF} > \tau_O$ the model is in the salinity oscillation regime. In this case the overturning circulation is so strong that the freshwater flux has almost no effect on the variations of the overturning circulation (ω'). At first order, the salinity variations are controlled by the the mean flow advection of the salinity perturbation gradient ($\overline{\omega}\partial_\phi S'$), inducing the salinity oscillations (solid arrows in Fig. 11). At second order, small variations of the overturning allow dipolar anomalies to be sustained through the freshwater flux (Fig. 10a).
- If $\tau_{SF} < \tau_O$ the model is in the salinity feedback regime. The surface freshwater flux is here strong enough to significantly impact the salinity over an overturning period, hence the overturning circulation itself (ω'). The variations of salinity anomalies are controlled by the anomalous advection of the mean salinity gradient ($\omega'\partial_\phi \overline{S}$). The mean flow advection, predominant in the previous case, is now negligible: salinity anomalies grow and modify the overturning before being advected around the overturning loop. This case results in the positive salinity feedback regime sketched with dashed arrows in Figure 11 (Marotzke, 1996).

When the freshwater forcing amplitude is continuously increased in the Howard-Malkus loop, the regimes found are, first, a stable thermally-driven steady state, which is later destabilized through a Hopf bifurcation with growing centennial salinity oscillations, and further on through a second bifurcation with a non-oscillatory unstable mode driven by the positive salinity feedback regime. Most importantly, this scenario is also found in time integrations of 2-D and 3-D models.

5. Bihemispheric pole-to-pole configuration

a. Pole-to-pole 2-D model

In this section we investigate the centennial mode in a more realistic bihemispheric basin extending from 66S to 66N (other parameters alike those given in Table 1). Because of the great uncertainty in the observed freshwater forcing, we first run the 2-D model with no convection under surface restoring boundary conditions for temperature and salinity (Fig. 12). This experiment leads to a first steady-state. The implied freshwater flux is diagnosed (Fig. 12) and used in the second experiment carried out under mixed boundary conditions, but the initial state is perturbed by -1°C ($+1$°C) in the northern (southern) hemisphere: the model settles in a pole-to-pole steady-state circulation revealing a strong overturning (around 24 Sv) with northern downwelling (Fig. 13). This procedure enables us

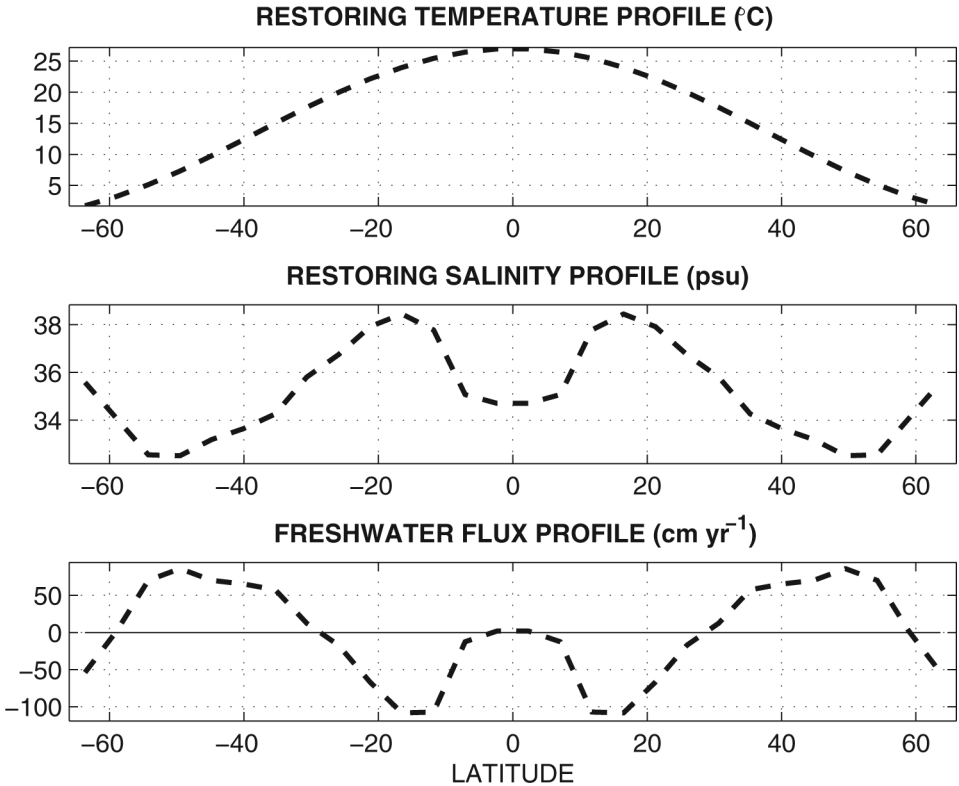

Figure 12. Forcing profiles in the bihemispheric configuration experiments. (top) Surface temperature restoring profile used for the bihemispheric configurations. (middle) Surface salinity restoring profile used to obtain the first bihemipheric steady state. (bottom) Freshwater flux diagnosed at the first bihemispheric steady-state under restoring surface boundary conditions for both temperature and salinity, and used for the subsequent bihemipheric experiments under mixed boundary condition.

to investigate the stability of a asymmetric bihemispheric circulation, but allows the salinity to evolve freely.

A linear stability analysis on this pole-to-pole steady state reveals a much longer oscillation period (733 yr) than previously, and strong damping (in 67 yr) (Fig. 13). The anomalies (whose density is strongly determined by salinity) seem to be passively advected by the mean circulation as observed in the single hemisphere configuration.

The upwelling region now extends on both hemispheres. Some of the salinity anomalies propagating southward at depth are brought back to the surface in the northern hemisphere, where they still experience a reinforcement through the surface freshwater fluxes, as described in the single hemispheric case. But, some among the salinity anomalies propagate down to the southern hemisphere (almost 10 Sv), and upwell in regions where the

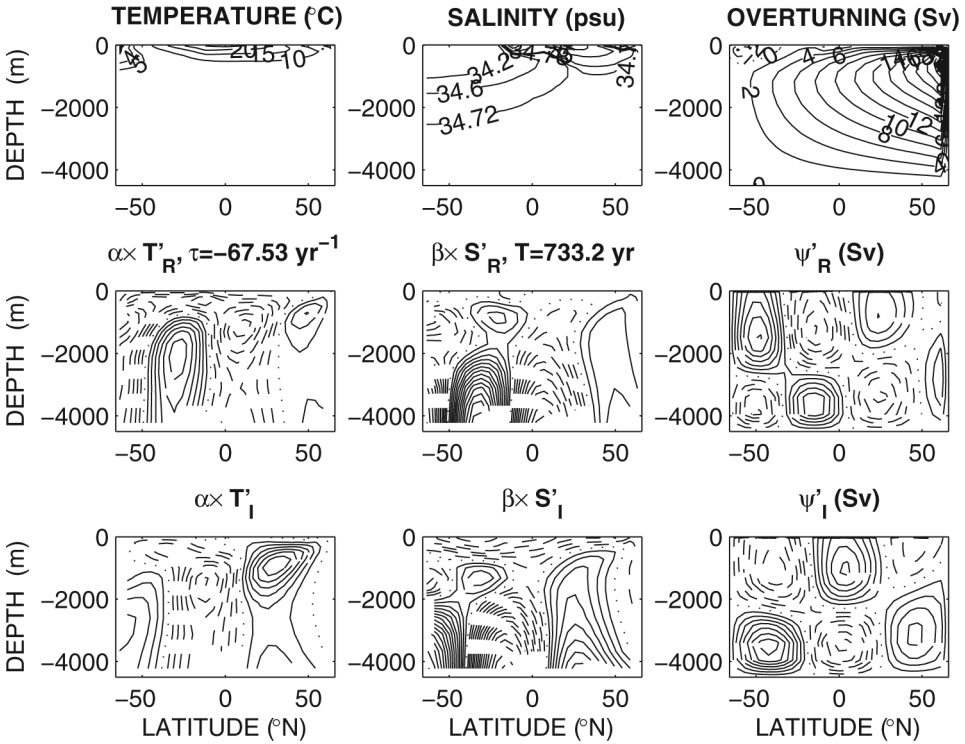

Figure 13. First row: temperature (°C), salinity (psu) and overturning (Sv) of the steady state in our bihemispheric model. Second and third rows: less damped oscillation from the linear stability analysis of the bihemispheric pole-to-pole experiment. The solid, dashed and dotted lines respectively correspond to the positive, negative and zero anomalies. The periodic time evolution is: $X_R \rightarrow X_I \rightarrow -X_R \rightarrow -X_I \rightarrow X_R$. The anomalies at depth seem to be passively advected around the main overturning loop. Note that the mode is damped, and its period is now 733 yr.

freshwater flux may no longer provide reinforcement but rather weaken the anomalies. The net impact on the anomalies may finally be insufficient to counterbalance other damping effects like diffusion.

Hence the eigenmode is quite different from the single-hemisphere one as it has, now, a wavenumber 2 structure along the mean streamfunction contours. A major difference with the one-hemisphere solution is also the oscillation period now increased to 733 yr. However, the maximum overturning is around 24 Sv for a basin of twice the volume of the one hemisphere, so that the renewal time of the water remains the same (here, basin volume-to-maximum overturning ratio $\sim$ 170 yr). These results may suggest a change in the physical mechanism between the two configurations.

As we can see in the density variance budget (Table 6) the bihemispheric pole-to-pole configuration introduces a strong diminution of the temperature forcing term which cannot

Table 6. As Table 4 for the bihemispheric pole-to-pole experiments: latitude-depth model (without and with Antarctic Circumpolar Current) and Howard-Malkus loop.

Two hemisphere:	Latitute-depth model		Howard-Malkus loop
Variance term	without ACC	with ACC	
Adv$(T', \overline{T})$	−0.00709	−0.0203	0.000646
Adv$(S', \overline{S})$	−0.00167	0.0104	0.000782
Adv$(T', \overline{S})$	0.00353	0.00669	−0.000402
Adv$(S', \overline{T})$	0.00649	−0.051	−0.00213
TotAdv	**0.00126**	**−0.0542**	**−0.0011**
Diff(T', T')	−0.0109	−0.00616	−0.00009
Diff(S', S')	−0.027	−0.0123	−0.00336
Diff(T', S')	0.0111	0.063	0.000184
Diff(S', T')	0.0111	0.063	0.000184
TotDiff	**−0.0157**	**−0.0119**	**−0.00309**
Forc(T', T')	−0.000106	−0.000112	−0.000461
Forc(T', S')	0.000697	−0.000416	0.00155
TotForc	**0.000591**	**−0.000528**	**0.00109**
Tot	**−0.0139**	**−0.0666**	**−0.0031**

counterbalance the high negative diffusive term, as it could be in the one hemispheric case (Table 6). The density variance budget, as our linear stability study, highlights the forcing to explain the damping of the centennial oscillation in this pole-to-pole configuration. We will now extend further the Howard-Malkus loop to a bihemispheric configuration, in order to better understand these changes in the structure and damping of the oscillatory eigenmode.

b. Howard-Malkus loop in bihemispheric configuration

Eqs. (20) are readily applicable to the bihemispheric case with only a modification of forcing geometries (I^T and I^S). Actually in the one hemispheric case, the atmospheric forcing is antisymmetric with respect to the middle latitude. In a bihemispheric case the forcing becomes symmetric with respect to the equator (Fig. 14). The renewal time of the water being the same in both cases, we will keep unchanged the frictional parameter (k) of the model.

The nonlinear time integration reveals damped oscillatory anomalies (Fig. 15) where density is salinity-dominated. The period of this oscillation is around 605 yr (Table 2).

As expected this experiment shows a strong modification of the centennial oscillation mechanism upon the shift from one- to two-hemisphere configuration. The only change between the two Howard-Malkus configurations is the geometry of the forcing; the slight variation in freshwater intensity (from 80 to 101 cm yr^{-1}) cannot explain such a big difference in the oscillation period. This geometry was previously shown to be of high importance for the oscillation growth and mechanism in the one-hemispheric case; so the issue now

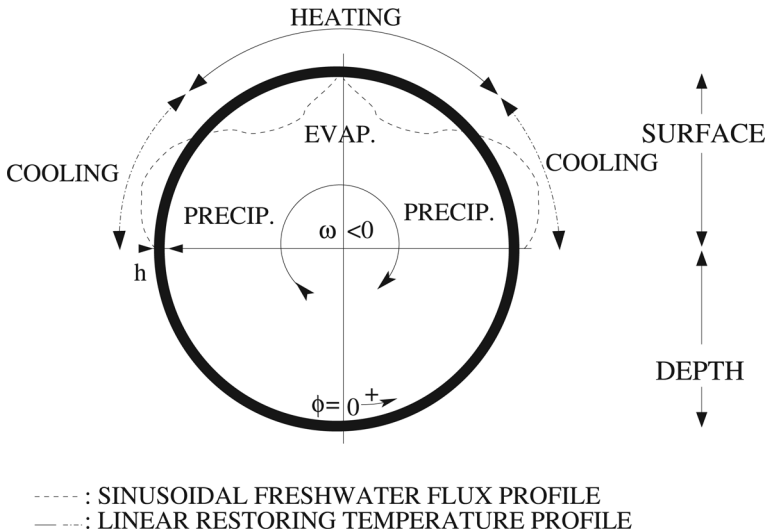

Figure 14. Bihemispheric configuration of the Howard-Malkus loop with symmetric forcing.

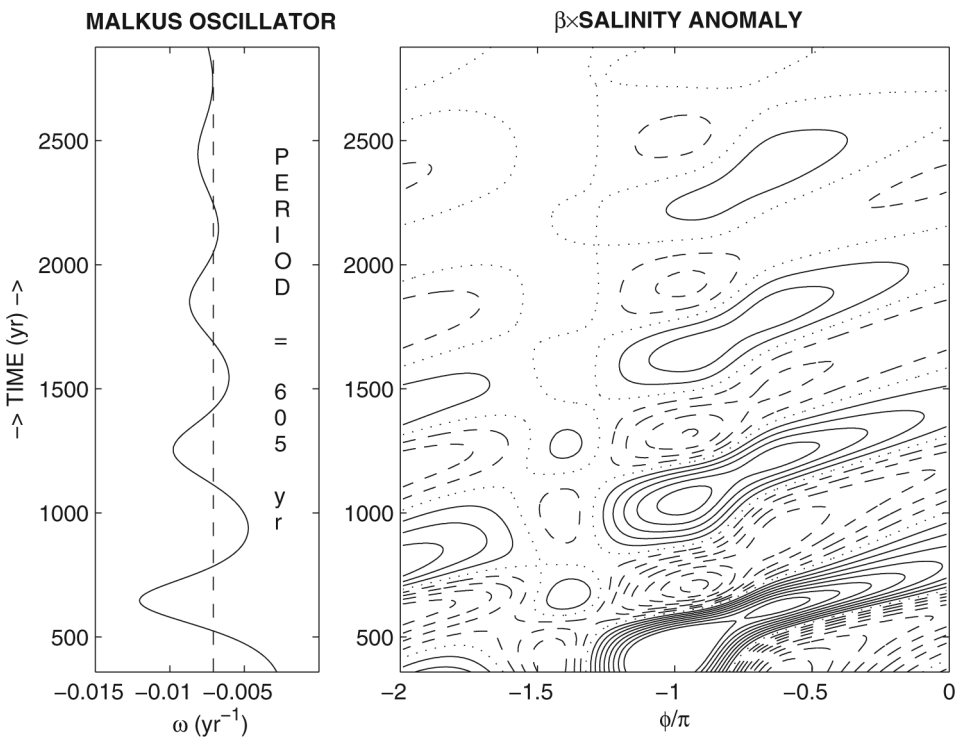

Figure 15. Nonlinear integration of the bihemipsheric Howard-Malkus loop model showing a damped oscillation of 605-yr period.

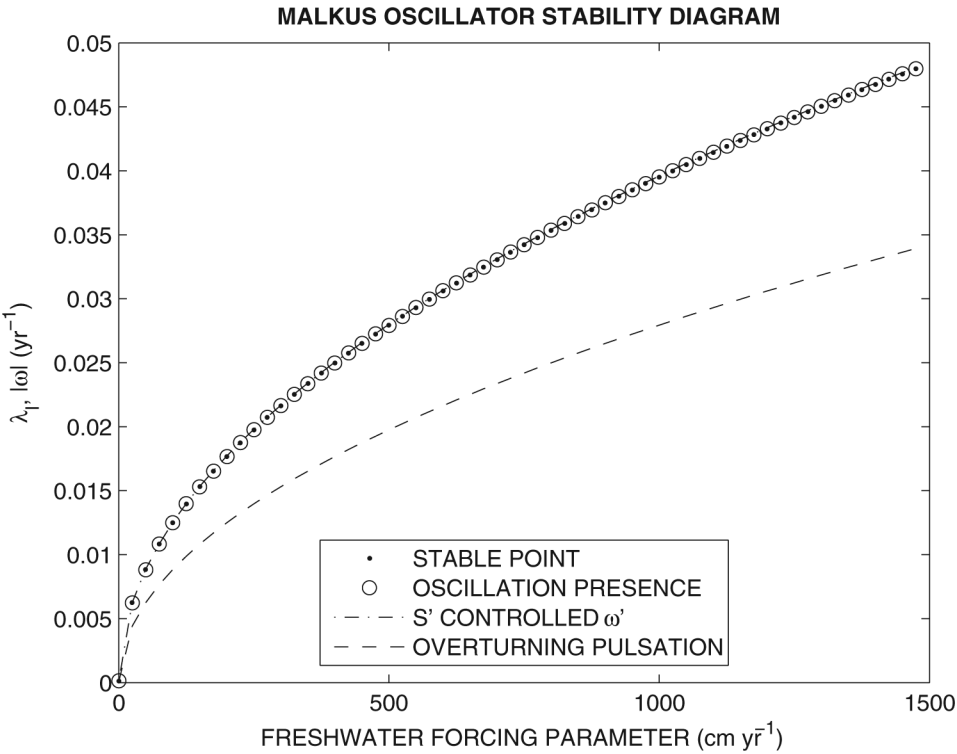

Figure 16. Stability diagram for the bihemispheric Malkus loop oscillator as a function of the freshwater intensity F_0 (up to very high, unrealistic, values). All the points are stable. The eigenmode with the largest real part is oscillatory. Dashed lines are the steady-state overturning pulsation in each case. The 'salinity-controlled overturning' subsystem is plotted in dash-dotted line.

is to understand why and how the period and growth of the centennial oscillations are so deeply modified by this new forcing geometry.

We will thus perform the same kind of analysis, through modal decomposition, as previously done to obtain the steady state (24a-d) and perturbations (26). This decomposition evidenced a strong modification of the steady state responsible for changes in the perturbations equations. The projection of the forcing now occurs on harmonics different from those in the one hemispheric case: I_i^T and I_i^S are canceled instead of I_r^T and I_r^S. As a result, the mean overturning $\overline{\omega}$ is controlled by salinity instead of temperature ($\overline{\omega} \simeq k\beta\overline{S_i}$).

Results for modes $n \neq 1$ are not modified (27). For $n = 1$, the diagram of stability shows a stable oscillatory branch (Fig. 16) really different from the one found in the one hemispheric case (Fig. 9). The oscillation period for a freshwater amplitude of 101 cm yr^{-1} is 502 yr, and is comparable to the one found for the bihemispheric pole-to-pole configuration with the 2-D model (733 yr).

Concerning the 'salinity-controlled overturning' subsystem, the symmetric geometry of the forcing ($I_i^S = 0$ induces $\overline{S_r} = 0$) leads to the following characteristic equation from (29) and (24c–d):

$$[\lambda^2 + \omega^2 + \omega k\beta\overline{S_i}][(\lambda + r_T)^2 + \overline{\omega}^2] = 0. \tag{36}$$

The second part of the equation leads to the complex conjugate solutions: $-r_T \pm i|\overline{\omega}|$. It corresponds to an oscillation at the overturning period with a strong damping rate $O(1\,\text{yr})$. The first part of the equation provides a purely oscillatory eigenmode (although the nonlinear time integration shows a damped oscillation, because of diffusion not considered in this calculation):

$$\lambda = i\sqrt{\overline{\omega}^2 + \frac{k\beta S_0 F_0 I_r^S}{h}}, \tag{37}$$

which corresponds to an oscillation period of 502 yr for a freshwater intensity worth 101 cm yr^{-1}. The control of overturning by salinity ($\overline{\omega} \simeq k\beta\overline{S_i}$) leads to the simple solution $\lambda \simeq i\sqrt{2}|\overline{\omega}|$. In this pole-to-pole configuration the period is no longer as close to $\overline{\omega}$ as in the one hemispheric case.

Unlike in the one hemispheric case, the growth of the anomaly is, here, impossible. Actually the decrease and increase of overturning by the anomalies are no longer correlated with the adequate forcing zone. As shown in Figure 17 the anomaly cannot be enhanced by the salinity feedback in a bihemispheric case. This result highlights the importance of the duality between the temperature-dominated steady flow and the impact of salinity-dominated

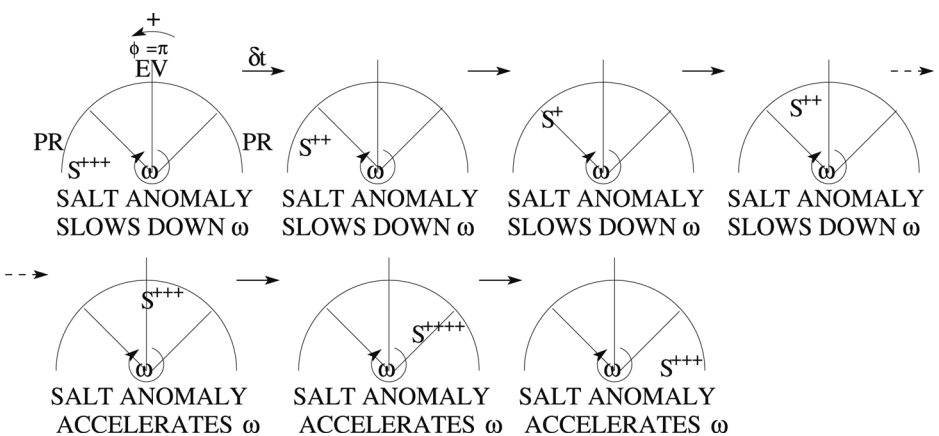

Figure 17. Schematic representation of the time evolution of salinity anomalies passing through the freshwater forcing zone and influencing the overturning ω in the bihemispheric case. Perturbation growth or decay is a function of the freshwater forcing configuration, here tropical evaporation and subpolar precipitation in both hemispheres. The perturbation decreases as much as it increases the overturning in each salinity forcing zone. Hence the perturbation does not experience a net increase. In a symmetric forcing case there is then no positive salinity feedback.

anomaly on the overturning. This duality does no longer exist in the bihemispheric configuration where the steady state and anomaly are both driven by salinity.

The density variance budget (Table 6) shows a negative total density variance due to a negative contribution of the advection.

c. Pole-to-pole case with ACC

To take into account the main source of north-south asymmetry in the global ocean circulation, let us now include a crude parametrization of the Antarctic Circumpolar Current (ACC) through the Drake passage, extending here from 62S to 40S and 2500 m deep. Because of the opening in this passage, a periodic boundary condition requires a null zonal pressure difference, and thus the dynamical equation (4) has to be modified; following Paillard and Cortijo (1999) we simply increase the local friction coefficient by a factor 1000 to substantially reduce the meridional velocities in the ACC.

The same restoring surface temperature, freshwater flux and initial fields from the previous experiment are used. The model settles into a steady state. A linear stability analysis allows us to identify the centennial oscillatory eigenmode as a damped oscillatory mode (Fig. 18). Anomalies in temperature and salinity are advected all around the North Atlantic overturning cell, and their density is dominated by salinity. Their structure is very close to the single hemisphere case. The oscillation period is 750 yr, which is more than twice the one in the single hemisphere experiment but close to the one in the pole-to-pole case. This damped oscillation is governed by the same mechanism as the one discussed in the previous pole-to-pole 2-D and loop models.

A density variance budget is again performed to quantify the damping mechanism of the oscillation in the last configuration (Table 6). The main difference between the cases with and without ACC is the contributions of advection and restoring surface temperature that become negative: hence the density variance is strongly damped.

d. Discussion

Such a centennial-scale oscillation where a large-scale salinity anomaly is advected all around the overturning cell has been presented in the Large-Scale-Geostrophic (LSG) global ocean model forced by mixed boundary conditions with stochastic noise added to the freshwater forcing (Mikolajewicz and Maier-Reimer, 1990). This study presents a compelling figure of zonally-averaged salinity anomaly in the Atlantic where a dipole propagates in a way very similar to our findings. This similarity seems to validate a posteriori our 2-D model approach; hence, for investigations on such long-period and large-scale oscillations the zonally-averaged model seems a valid simplification.

More recently, Weijer and Dijkstra (2003) described a damped oscillation through a linear stability analysis of a global 3-D ocean model: its pattern resembles ours except that the dipole anomalies are advected over the whole conveyor belt across the Antarctic Circumpolar Current and Pacific Ocean. Their study reported on a similar scale for thermal

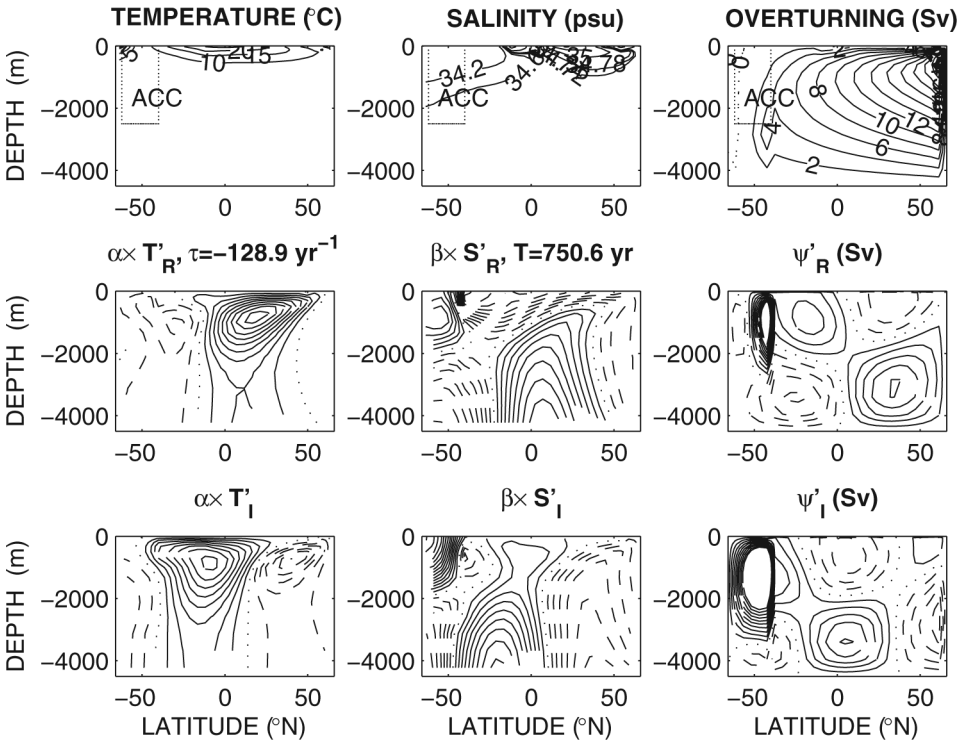

Figure 18. As in Figure 13 for the asymmetric configuration with ACC. The anomalies seem to be passively advected around the main overturning loop in the northern basin. The oscillatory eigenmode, which period is 750 yr, is damped.

and haline anomalies, but gave no clue about the dominant term. However, their 3-D model remains very frictional, and may not differ too much from our 2-D approximation.

6. Conclusion

This study discussed the stability of simplified models of the oceanic thermohaline circulation able to reproduce the centennial scale oscillations found in 3-D models. We used a 2-D latitude-depth model based on planetary geostrophic dynamic. By considering, first, a single-hemisphere basin configuration under mixed boundary conditions, we observed centennial oscillations with a density signature more intense in salinity than in temperature. A linear stability analysis revealed the same centennial oscillation. A density variance budget provided an objective way to identify the sources of variance sustaining the oscillations against dissipation, i.e. the temperature restoring term, through well-correlated temperature and salinity anomalies likely associated with changes in the overturning.

To get the roots of the oscillation mechanism, we also used an even more simplified model constituted by the 1-D Howard-Malkus loop oscillator. Through various cases tractable

analytically, we characterized the different regimes and damping processes of oscillation. We found that the period is set by the mean overturning advection. At first order, salinity anomalies are purely advected by the mean overturning flow. The mechanism sustaining this oscillation enters at second order, it is close to the traditional positive salinity feedback. Growing salinity oscillations and positive salinity feedback correspond to a different regime of the same mechanism ruled by the model parameters, namely, the characteristic time scale of the overturning and the response time of the overturning to the salinity forcing. Below a threshold for the freshwater flux, oscillations are possible because salinity anomalies are advected by the mean flow faster than reinforced by the freshwater flux (through the anomalous advection of the mean salinity gradient). Above the threshold, reinforcement of salinity anomalies and subsequent modifications of the overturning overwhelm the mean flow advection and lead to the positive feedback.

Maybe in contrast with the 2-D model, the density variance budget in the Howard-Malkus loop suggests an internal instability connected to the correlation of salinity and overturning anomalies. In fact, depending on the surface temperature relaxation strength, the forcing contribution to the density variance of the centennial oscillations can be either positive (for the case most similar to the two-dimensional model) or negative (stronger relaxation). These considerations made us suggest that the salinity-overturning oscillator mechanism applies to the 2-D case, but requires some help from the surface temperature relaxation to be sustained against the dissipation. The tracer diffusion is certainly the most active damping term, as already shown for interdecadal oscillations (Huck *et al.*, 1999a).

At last, the configuration of our 2-D model is adapted to a single basin extending on the two hemispheres. Oscillations are no longer sustained through the nonlinear model integration. Linear stability analyzes performed at various pole-to-pole steady states, with and without a parametrization of the Antarctic Circumpolar Current through the Drake passage, showed damped eigenmodes with spatial structures very similar to the ones found in a single hemisphere. These last results confirm that the centennial oscillation is more heavily damped and cannot persist in such a bihemispheric configuration. The Howard Malkus loop analysis extended to this two-hemisphere configuration suggests that the symmetric surface forcing strongly damps the oscillations, but also largely increases the oscillation period (fundamentally the steady state overturning is no longer thermally- but salinity-driven). These oscillations would need strong stochastic noise in the atmospheric forcing to be continuously excited (Mysak *et al.*, 1993). These results are in agreement with experiments in 3-D global ocean models (Mikolajewicz and Maier-Reimer, 1990; Weijer and Dijkstra, 2003) showing that (i) the centennial mode structure and mechanism are well captured in a zonally-averaged 2-D ocean model, and (ii) the centennial mode is strongly damped and requires stochastic forcing to be excited.

The mechanism and signature of the centennial oscillation now being clearly identified in simplified models, they need to be tested in 3-D realistic global models in order to determine their most realistic patterns and growth or damping rate. Given the critical role of the surface relaxation for the oscillation damping or growth, this oscillation mechanism

should be tested in more realistic ocean models coupled with atmospheric models, eventually simplified like energy balance model ones. The salinity being the essential density variable for the oscillation, the coupling with sea-ice would be worth considering given its influence on the freshwater flux and air-sea interactions. These studies should give more insight into the robustness of this centennial oscillation and into its possible relevance for observed or future climate variability.

Acknowledgments. Thorough proofreadings, corrections and suggestions by Alain Colin de Verdière, Henk Dijkstra, and especially Jochem Marotzke, are gratefully acknowledged and have significantly streamlined and clarified the original manuscript.

REFERENCES

Arzel, O. 2004. Mécanismes de variabilité climatique interdécennale dans des modèles idéalisés. Ph.D. thesis, Université de Bretagne Occidentale, Brest, France, 240 pp.

Arzel, O., T. Huck and A. Colin de Verdière. 2006. The different nature of the interdecadal variability of the thermohaline circulation under mixed and flux boundary conditions. J. Phys. Oceanogr., (in press).

Colin de Verdière, A. and T. Huck. 1999. Baroclinic instability: an oceanic wavemaker for interdecadal variability. J. Phys. Oceanogr., *29*, 893–910.

Dewar, W. K. and R. X. Huang. 1995. Fluid flow in loops driven by freshwater and heat fluxes. J. Fluid Mech., *297*, 153–191.

——— 1996. On a forced flow of salty water in a loop. Phys. Fluids, *4*, 954–970.

Dijkstra, H. and M. J. Molemaker. 1997. Symmetry breaking and overturning oscillations in thermohaline-driven flows. J. Fluid Mech., *4*, 169–198.

Howard, L. N. 1971. ABC's of convection. Geophysical Fluid Dynamics Summer Program. Tech. Rep., 71-63, 102-105, WHOI internal report.

Huang, R. X. 1993. Real freshwater flux as a natural boundary condition for the salinity balance and thermohaline circulation forced by evaporation and precipitation. J. Phys. Oceanogr., *23*, 2428–2446.

Huang, R. X. and W. K. Dewar. 1996. Haline circulation: bifurcation and chaos. J. Phys. Oceanogr., *26*, 2093–2106.

Huck, T., A. Colin de Verdière and A. J. Weaver. 1999a. Interdecadal variability of the thermohaline circulation in box-ocean models forced by fixed surface fluxes. J. Phys. Oceanogr., *29*, 865–892.

Huck, T. and G. K. Vallis. 2001. Linear stability analysis of three-dimensional thermally-driven ocean circulation : application to interdecadal oscillations. Tellus, *53A*, 526–545.

Huck, T., A. J. Weaver and A. Colin de Verdière. 1999b. On the influence of the parameterization of lateral boundary layers on the thermohaline circulation in coarse-resolution ocean models. J. Mar. Res., *57*, 387–426.

Jones, P. D. and M. E. Mann. 2004. Climate over past millennia. Rev. Geophys., *42*, RG2002, doi: 10.1029/2003RG000 143.

Keller, J. B. 1966. Periodic oscillations in a model of thermal convection. J. Fluid Mech., *26*, 599–606.

Lorenz, E. N. 1955. Available potential energy and the maintenance of the general circulation. Tellus, *VII*, 157–167.

Maas, L. R. M. 1994. A simple model for the three-dimensional, thermally and wind-driven ocean circulation. Tellus, *46A*, 671–680.

Malkus, W. V. R. 1972. Non-periodic convection at high and low Prandtl number. Mémoires Société Royale des Sciences de Liège, 6^e Serie, Tome IV, 125–128.

Marotzke, J. 1996. Analysis of thermohaline feedbacks, *in* Decadal Climate Variability: Dynamics and Predictability, D. L. T. Anderson and J. Willebrand, eds., NATO ASI Series, Series I, *44*, 333–378.

Marotzke, J. and J. R. Scott. 1999. Convective mixing and the thermohaline circulation. J. Phys. Oceanogr., *29*, 2962–2970.

Marotzke, J., P. Welander and J. Willebrand. 1988. Instability and multiple steady states in a meridional-plane model of the thermohaline circulation. Tellus, *40A*, 162–172.

Mikolajewicz, U. and E. Maier-Reimer. 1990. Internal secular variability in an ocean general circulation model. Climate Dyn., *4*, 145–156.

Mysak, L. A., T. F. Stocker and F. Huang. 1993. Century-scale variability in a randomly forced, two-dimensional thermohaline ocean circulation model. Climate Dyn., *8*, 103–106.

Paillard, D. and E. Cortijo. 1999. A simulation of the Atlantic meridional circulation during Heinrich event 4 using reconstructed sea surface temperatures and salinity. Paleoceanography, *14*, 716–724.

Quon, C. and M. Ghil. 1995. Multiple equilibria and stable oscillations in thermosolutal convection at small aspect ratio. J. Fluid Mech., *291*, 33–56.

Stocker, T. F. and L. A. Mysak. 1992. Climatic fluctuations on the century time scale: a review of high-resolution proxy data and possible mechanisms. Clim. Change, *20*, 227–250.

Stommel, H. 1961. Thermohaline convection with stable regimes flow. Tellus, *13*, 224–230.

Te Raa, L. A. and H. A. Dijkstra. 2002. Instability of the thermohaline ocean circulation on interdecadal timescales. J. Phys. Oceanogr., *32*, 138–160.

——— 2003. Modes of internal thermohaline variability in a single-hemispheric ocean basin. J. Mar. Res., *61*, 491–516.

Tziperman, E. *et al.* 1994. Instability of the thermohaline circulation with respect to mixed boundary-conditions: Is it really a problem for realistic models? J. Phys. Oceanogr., *24*, 217–232.

Weaver, A. J., E. S. Sarachik and J. Marotzke. 1991. Freshwater flux forcing of decadal and interdecadal oceanic variability. Nature, *353*, 836–838.

Weijer, W. and H. A. Dijkstra. 2003. Multiple oscillatory modes of the global ocean circulation. J. Phys. Oceanogr., *33*, 2197–2213.

Welander, P. 1957. Note on the self-sustained oscillations of a simple thermal system. Tellus, *IX*, 419–420.

——— 1965. Steady and oscillatory motions of a diffentially heated fluid loop. Tech. Rep., 65-48, Woods Hole Oceanographic Institution, 34 pp.

——— 1967. On the oscillatory instability of a differentially heated fluid loop. J. Fluid Mech., *29*, 17–30.

——— 1986. Thermohaline effects in the ocean circulation and related simple models, *in* Large-scale Transport Processes in Oceans and Atmosphere, D. L. T. Anderson and J. Willebrand, eds., 163–200.

Winton, M. and E. S. Sarachik. 1993. Thermohaline oscillations induced by strong steady salinity forcing of ocean general circulation models. J. Phys. Oceanogr., *23*, 1389–1410.

Wright, D. G. and T. F. Stocker. 1991. A zonally averaged ocean model for thermohaline circulation. Part I : model development and flow dynamics. J. Phys. Oceanogr., *21*, 1713–1724.

Wright, D. G., T. F. Stocker and D. Mercer. 1998. Closures used in zonally averaged ocean models. J. Phys. Oceanogr., *28*, 791–804.

Wright, D. G., C. B. Vreugdenhil and T. M. Hughes. 1995. Vorticity dynamics and zonally averaged ocean circulation models. J. Phys. Oceanogr., *25*, 2141–2154.

Zhang, S., C. A. Lin and R. J. Greatbatch. 1992. A thermocline model for ocean-climate studies. J. Mar. Res., *50*, 99–124.

Received: *4 August, 2004;* revised: *9 February, 2006*.